CFD SIMULATION OF THE HYDRODYNAMICS AND REACTION KINETICS OF CHEMICAL LOOPING COMBUSTION PROCESS IN A FUEL REACTOR

Chen L.[a], Yang X.[a,*], Li X.[b], Snape C.[b]
*Author for correspondence
[a]International Doctoral Innovation Centre (IDIC)
The University of Nottingham Ningbo
University Park, Ningbo 315100, P.R. China

[b]Faculty of Engineering, The University of Nottingham
University Park, Nottingham NG7 2RD, UK
Email: xiaogang.yang@nottingham.edu.cn

ABSTRACT

A typical CLC unit consists of a circulating fluidised bed as the air reactor and a bubbling fluidised bed as the fuel reactor. A number of studies on the hydrodynamics behaviours of the CLC process in fuel reactor have been documented in the open literature and some are focused on numerical modelling of dynamic processes in the fuel reactors but 3D numerical modelling of the multiphase flow coupled with chemical reaction dynamics in the fuel reactor is still rarely undertaken. This paper aims to investigate the CLC process in a fuel reactor using the 3D-CFD modelling, coupled with the heterogeneous reactions, the hydrodynamics and reaction kinetics of the CLC process in the fuel reactor. A parameter used for relating the time-dependent bubble occurance to the local eddies is proposed by correlating the local velocity fluctuation with the pressure fluctuation. The relation between the concentration of gaseous reactants or products and local vortices is also investigated. The results obtained clearly indicate that the CFD modelling conducted in the current study reasonably forecasts the hydrodynamic behaviours and important phenomena observed in the fuel reactor. The parameter correlating the bubble occurabce with local velocity fluctuation may be used in the CLC for controlling the bubbling phenomenon because the occurrence of the bubbles at specific positions is strongly associated with the locally embedded large eddies.

INTRODUCTION

The fact that chemical looping combustion (CLC) can be used as a potential alternative to reduce the industrial CO_2 emission has been well recognised. The inherent separation process of CO_2 from other combustion products like N_2 and exceeded O_2 involved in the CLC can effectively minimise the energy penalty encountered when using other CO_2 capture and storage (CCS) technologies. CLC process divides the traditional combustion reaction into two serial reactions including an oxidation and a reduction. Oxygen carriers (OCs), usually the metal oxides with high reactivity, are employed to maintain the solid circulation between the fuel reactor where the reduction of OCs is taking place with the gaseous products of CO_2 and H_2O and the air reactor where oxygen carriers are regenerated with the air. Until very recently, the small scale CLC plants varied from 300W to 140kW have been constructed for demonstration. It was revealed that Cu-based oxygen carriers may have a potential because of its high chemical reactivity, large oxygen transfer capacity and no thermodynamic restriction on the complete conversion of fuels into CO_2 and H_2O. Adánez *et al.* [1] tested CuO/Al_2O_3 in a 10kW CLC system with the gaseous fuel of methane and have found that the ratio of oxygen to fuel and fuel reactor temperature play important roles on the combustion efficiency. Similar conclusion was also obtained using the CLC system with syngas as the fuel [2]. In addition, high attrition resistance and no carbon deposition were observed in the trial running. Meanwhile, the relatively cheaper price of Cu-based oxygen carriers and less environmental risk also increase the possibility of commercial applications, compared with Co-based and Ni-based oxygen carriers.

The use of CFD modelling has been considered as an economical option to optimise the design, to improve the performance and to investigate how to scale up in the CLC design. It has now become more and more popular to employ CFD modelling to replace the expensive experimental investigations. As CFD method can provide a connection between the hydrodynamic process of the CLC and chemical reactions, it can provide physical insight into the complicated phenomena encountered in the CLC process, particularly in fuel reactor with different fuels and oxygen carriers, as evidenced in [3-7]. A similar result obtained from the above simulations was that the bed temperature had a significant influence on the combustion efficiency of the fuel, which was also observed in the experiments [1, 8].

In the present study, 3-D CFD simulations aimed at describing the flow behaviours of the fuel reactor including the hydrodynamics and chemical kinetics are conducted. The data derived from the experiments of Forero *et al.* [8] are used to validate the CFD model. CuO impregnated on Al_2O_3 will be used as the oxygen carriers with methane as the fuel, the same as described in [8]. It is expected that the CFD model validated herein can be used to optimise the operation of the CLC unit. The correlation parameters proposed for describing the bubble occurrence in 2-D fuel reactor [9] will be employed and extended to 3-D fuel reactor model.

NOMENCLATURE

C	[Mol/m^3]	Bulk concentration of gaseous reactant
$\mathbf{C}$	[m/s]	Fluctuating velocity of particles
C_D	[-]	Drag coefficient of drag model
d_p	[m]	Diameter of particle
e	[-]	Coefficient of restitution
E_0	[kJ/mol]	activation energy
$\boldsymbol{g}$	[m/s^2]	Acceleration due to gravity
g_0	[-]	Radial distribution function
h_{sg}	[W/m^{2}K]	Heat transfer coefficient between gas and solid phase
H	[J/kg]	Enthalpy
$\boldsymbol{I}$	[-]	Unit tensor
$\boldsymbol{I}_{2D}$	[s^{-2}]	Second invariant of the deviatoric stress tensor
$\boldsymbol{J}_{i,j}$	[kg/m^2]	Diffusive mass flux
k	[W/mK]	Thermal conductivity
k_0	[$mol^{1-n}m^{3n-2}s^{-1}$]	Reaction pre-exponential factor
m'_{pq}	[kg/m^{3}s]	Mass transfer from the p_{th} to q_{th} phase
Nu	[-]	Nusselt number
Pr	[-]	Prandtl number
p	[N/m^2]	Gas pressure
P_s	[N/m^2]	Solid pressure
Q_{pq}	[W/m^2]	Interphase Heat transfer from the p phase to q phase
r_g	[m]	Mean radius of the grain
R	[JK^{-1}mol^{-1}]	Universal gas constant
R_{he}	[kmol/m^{3}s]	Heterogeneous reaction rate
$\boldsymbol{u}$	[m/s]	Velocity
X	[-]	Conversion
$Y_{i,j}$	[-]	Mass fraction of species *j* in phase *i*
Special characters		
α_{time}	[-]	Time correlation parameter
α	[-]	Volume fraction
ρ	[kg/m^3]	Density
ρ_m	[mol/m^3]	Molar density of the particle
μ_g	[N.s/m^2]	Dynamic viscosity for gas phase
μ_s	[kg/ms]	Solid shear viscosity
β	[kg/m^{3}s]	gas-solid interphase exchange coefficient
λ_p	[N s/m^2]	Gas or solid bulk viscosity
$\boldsymbol{\tau}_i$	[N/m^2]	Stress tensor of i_{th} phase
Θ_s	[m^2/s^2]	Granular temperature
$\boldsymbol{\Phi}$	[kg/ms^2]	Exchange of fluctuation energy
γ	[kg/ms^3]	Dissipation rate
ξ	[-]	Angle of internal friction

MATHMATIC MODELLING

In the present analysis, Eulerian-Eulerian model was employed to model both the gas and sold phases with the kinetic theory of granular flow for the closure of solid phase. Governing equations and relations that have been employed in this study were documented in Table 1.The commercial CFD software ANSYS FLUENT 15.0 was adopted for the simulations. For simplification, solid particles are assumed to be spherical and have uniform distributions in density and size.

Table 1 Governing equations and relations of the systems employed in Eulerian-Eulerian model

The Continuity Equations

$$\frac{\partial}{\partial t}\left(\alpha_p\rho_p\right)+\nabla\cdot\left(\alpha_p\rho_p\boldsymbol{u}_p\right)=\dot{m}_{pq} \tag{1}$$

Momentum Balance Equations

$$\begin{aligned}&\frac{\partial}{\partial t}\left(\alpha_p\rho_p\boldsymbol{u}_p\right)+\nabla\cdot\left(\alpha_p\rho_p\boldsymbol{u}_p\boldsymbol{u}_p\right)=-\alpha_p\nabla p\\&+\nabla\tau_p+\alpha_p\rho_p\boldsymbol{g}-\beta(\boldsymbol{u}_p-\boldsymbol{u}_q)+\dot{m}_{pq}\boldsymbol{u}_p\end{aligned} \tag{2}$$

Gas and Sold Tensor Equations

$$\boldsymbol{\tau}_p=\mu_p((\nabla\boldsymbol{u}_p+(\nabla\boldsymbol{u}_p)^T)-\frac{2}{3}(\nabla\cdot\boldsymbol{u}_p)\boldsymbol{I})+\lambda_p(\nabla\cdot\boldsymbol{u}_p)\boldsymbol{I} \tag{3}$$

Energy equations

$$\frac{\partial}{\partial t}\left(\alpha_p\rho_pH_p\right)+\nabla\cdot\left(\alpha_p\rho_p\boldsymbol{u}_pH_p\right)=\nabla\cdot(k_p\nabla T_p)+Q_{pq}+\dot{m}_{qp}H_p \tag{4}$$

$$Where,\ Q_{pq}=h_{pq}(T_q-T_s),\quad h_{sg}=\frac{6k_g\alpha_s\alpha_gNu}{d_S^2} \tag{5}$$

Species transport equations:

$$\frac{\partial}{\partial t}\left(\alpha_i\rho_iY_{i,j}\right)+\nabla\cdot\left(\alpha_i\rho_i\boldsymbol{u}_iY_{i,j}\right)=-\nabla\cdot(\alpha_i\boldsymbol{J}_{i,j})+R_{he} \tag{6}$$

Drag Model

$$\beta=\frac{3\alpha_s\alpha_g\rho_g}{4v_{r,p}^2d_p}C_D\left|\mathrm{u}_s-\mathrm{u}_g\right| \tag{7}$$

Kinetic Theory of Granular Flow (KTGF)

$$\begin{aligned}&\frac{3}{2}\left[\frac{\partial}{\partial t}\left(\alpha_s\rho_s\Theta\right)+\nabla\cdot\left(\alpha_s\rho_s\boldsymbol{u}_g\Theta\right)\right]=\\&\left(-\nabla P_s\boldsymbol{I}+\boldsymbol{\tau}_s\right):\nabla\boldsymbol{u}_s+\nabla\cdot(k_{\Theta s}\nabla\Theta)-\gamma_s+\Phi_s+D_{gs}\end{aligned} \tag{8}$$

Hydrodynamic Model

The continuities of gas and solid phases accounting for the mass transfer due to the heterogeneous reaction are expressed by Equation (1) with *p*,*q*=g (gas) or *s* (solid phase). The sum of the volume fraction of each phase equals 1.0. The momentum equations for both phases are given by Equation (2). To ensure the closure of the governing equation, constitutive closure model (Tensors of the gas and solid) as defined by Equation (3) was adopted. The energy balances of both phases are described by (4). Q_{pq} accounting for the inter-phase heat transfer can be described by (5). The species transport is expressed using

Equation (6). The modified Syamlal-O'Brien drag model based on the experimentally minimum fluidization conditions, as expressed by Equation (7), is employed throughout the simulations as it could eliminate the over/under-prediction of the bed expansion encountered in the original Syamlal-O'Brien model. Finally, transportation of the solid fluctuating energy based on the kinetic theory of granular flow (KTGF) is described by Equation (8) with the granular flow temperature being defined as $\Theta = \langle C^2 \rangle /3$ used to describe the solid phase stresses and viscosities.

Chemical Kinetic Model

It has been found from experiments that the primary gaseous products of the reduction between Cu-based oxygen carrier and methane in the fuel reactor are mainly CO_2 and H_2O while CO and H_2 can be regarded as the intermediate products. As the concentration of CO and H_2 in the fuel reactor is quite low, the overall reaction is assumed and adopted in the CFD modelling for simplicity. Those kinetic parameters used in Equation (9) is listed in Table 2 [10]. The parameters of the shrinking core model employed are derived based on the experimental data produced in a thermo-gravimetric analyser (TGA) which can provide the excess reacting gas and reaction time. The relationship between the CH_4 conversion and the ratio of the inlet CH_4 concentration to CH_4 concentration in TGA test, derived from the experimental data of Forero [8], is shown in Figure 1 and used in our CFD modelling for CLC processes. It can be seen clearly from Figure 1 that incomplete combustion of CH_4 occurs when the ratio is greater than 2.2. A modification on the kinetic model based on the experimental outlet CH_4 concentration is introduced to provide more accurate description of the reaction rate in the fuel reactor. The modified shrinking core model is described by Equation (10). Table 3 Comparison of the outlet methane concentration between shrinking core model and modified shrinking core model shows a very good agreement between the experimental data and the computed outlet CH_4 concentration when using the modified shrinking core model for the reduction of CuO/Al_2O_3 with CH_4 at 1073K.

$$\begin{gathered} CH_4 + 4CuO \leftrightarrow 4Cu + CO_2 + 2H_2O \\ \Delta H_r = -178 kJ/mol \end{gathered} \tag{9}$$

$$\frac{dX}{dt} = \begin{cases} \dfrac{3bC^n k_0 \exp(-E_0/RT)}{\rho_m r_g}(1-X)^{2/3} & for\ 2.20 \le CH_4/CH_{4\_ref} < 3 \\ \dfrac{3bC^n k_0 \exp(-E_0/RT)}{\rho_m r_g}(1-X)^{2/3} \times 2.1175 e^{-0.34 CH_4/CH_{4\_ref}} & for\ CH_4/CH_{4\_ref} < 2.20 \end{cases} \tag{10}$$

Table 2 Kinetic parameters for CU-based oxygen carrier

	CH_4
r_g (m)	2×10^{-7}
ρ_m (mol/m^3)	8.06×10^4
b	4
k_0 (mol^{1-n}m^{3n-2}s^{-1})	30.0
E_0 (kJ/mol)	106
n	0.5

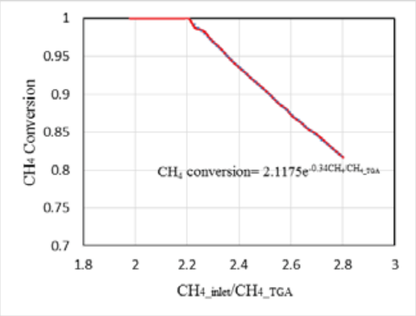

Figure 1 CH_4 conversion vs the ratio of inlet CH_4 concentration to the CH_4 concentration in TGA

Table 3 Comparison of the outlet methane concentration between shrinking core model and modified shrinking core model

Oxygen carrier to fuel ratio	Experimental value	Simulation value （shrinking core model）	Simulation value (modified shrinking model)
1.25	0.015	0.009	0.015
1.38	0.001	0.0035	0.035
1.5	0	0.003	0.003

Geometric model, initial and boundary conditions

The physical properties and operating parameters of the system employed in the simulation are summarised in Table 4. The reactor is assumed to be adiabatic. The grid of the fuel reactor was shown in Figure 1. Johnson and Jackson's slip boundary condition was imposed on the wall of the reactor [11], as indicated by Equations (11) and (12). Velocity inlet boundary condition and pressure outlet boundary condition were applied, respectively, to the inlet and exit of the fuel reactor. The phase coupled SIMPLE algorithm was employed to describe the pressure-velocity coupling of both gas and solid phases. The second order QUICK scheme was employed for calculation of those convective terms. In the simulation, grid independence test has been undertaken and it was found that the grid with the number of 225000 was able to reasonably predict the flow behaviours and concentration distribution of both gas and solid phases. Further refinement of grid has negligible impact on the simulation results.

$$n \cdot \tau_c = \frac{\sqrt{3\Theta}\pi\Phi\rho_s\alpha_s g_0 U_{sl}}{6\varepsilon_{s,\max}} \tag{11}$$

$$-n \cdot q = \frac{\sqrt{3\theta}\pi\Phi\rho_s\alpha_s g_0 |U_{sl}|^2}{6\alpha_{s,max}} + \frac{\sqrt{3}\pi\rho_s\alpha_s g_0 (1-e_w^2)\Theta^{3/2}}{4\alpha_{s,max}} \tag{12}$$

Table 4 Physical properties and operation parameters

Width of Bed (mm)	50.0
Height of Bed (mm)	100.0
Temperature (K)	1023.0
Viscosity of Nitrogen (g/cm .s)	2.3×10^{-4}
Inlet Fuel Gas Velocity (cm/s)	14.0
Diameter of Catalyst(μm)	370
CuO content (%)	14.0
Porosity of CuO/Al_2O_3 (%)	50.5
Density of Particle (kg/m^3)	1800
Minimum Fluidization Velocity(m/s)	0.056
Initial Solid Height(m)	0.6
Initial Solid Volume Fraction	0.55
Restitution Coefficient(e)	0.9
Wall Restitution Coefficient(e_w)	1.0
Specularity Coefficient Φ	0.6
Time Interval (s)	$10^{-3} – 10^{-5}$

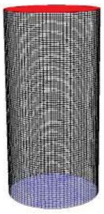

Figure 2. Grid imposed for the fuel reactor

RESULTS AND DISCUSSION

Bubble formation and distribution of reactants and products in the fuel reactor

In the presented study, the transient simulations of CLC process in the fuel reactor were carried out over a period of 12s. Initially, the Cu-based oxygen carriers are suspended and subsequently fluidised by the inert gas (pure N_2) introduced from the bottom of the fuel reactor. The feed gaseous fuel composed of CH_4 and N_2 wasn't fed into the fuel reactor until 3s. The methane is then oxidised by the oxygen contained in the CuO/Al_2O_3 with the productions of CO_2 and H_2O. Figure 3a shows the distribution of solid phase volume fraction at 10.3s and it well captures the characteristics of the gas-phase bubbles where the solid volume fraction is lower than its adjacent regions in the fuel reactor. The large gas-phase bubbles may cause a poor mixing between gas and solid phase and allow the combustible fuel bypass the dense bed without reacting with the oxygen carriers so that the conversion rate is reduced [3, 5]. Combining 4a and 3b, the mass fraction of methane is relatively higher in the gas-phase bubble region, indirectly indicating the aforementioned deduction. As presented in Figure 3 a, b and c, the mass fraction of CH_4 gradually decreases along the longitudinal direction when referencing from the distributor of the fuel reactor while the mass fraction of gaseous products complies with the reverse trend, according with the results obtained by Adanez *et al.* [12]. Figure 4a and b show, respectively, the contour plot of the gas-phase volume fraction and gas-phase velocity vector. It can be seen from the figure that a large eddy exists in the centre of the gas-phase bubbles in the dense bed, indicating the strong coupling between the bubble formation and the local eddies.

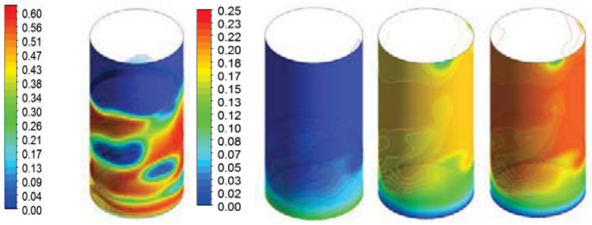

(a) (b) (c) (d)

Figure 3. Instantaneous contours of a) the volume fraction of the solid phase; b) mass fraction of CH_4; c) mass fraction of H_2O; d) mass fraction of CO_2 at 10.3s

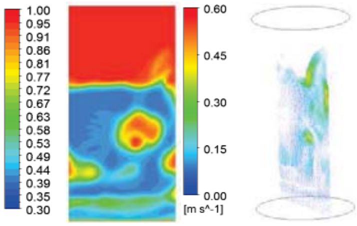

(a) (b)

Figure 4. (a) Instantaneous contour of gas phase volume fraction; (b) velocity vector of gas phase of y-z plane at 10.3s

Redistributions of reactants and products and dynamic parameters variations in fuel reactor

Figure 5 shows the time evolution of the mass fractions of CH_4, H_2O and CO_2 over a period of 9s starting at t=3s. It is obvious that the mass fractions of gaseous species ocillicate around a specific value with the elapsed time, indicating the CLC flow reaches a qusi-steady status. It can be seen from Figure 5a that the variation of the mass fraction of CH_4 falls into a value around 0.0015 after t=3.8s while those peak values is resulted from the fast by-pass gas-phase bubbles containing relatively higher concentration reacting gas, being consistent with the contour plots shown in Figure 3. The trend of changes of mass fractions of gaseous products such as H_2O and CO_2 are similar to that of CH_4, oscillating around the mean values of 0.17 and 0.21, respectively. Figure 6a presents the comparison of the simulated CH_4 concentration at the outlet with the experimental data of Forero *et al.* [8] by varying the ratio of oxygen carrier to fuel. Figure 6b compares the computed fuel combustion efficiency with the experiment results at 1073K. The maximum error between the simulation and experimental values is smaller than 1.25%. As shown in Figure 6 a, the simulated results reasonably capture the trend that the experimental CH_4

concentration at the outlet decreases gradually with increase of the ratio of oxygen carrier to fuel, eventually reaching the status of complete combustion. The simulation could well predict the outlet CH_4 concentration when the ratio of oxygen carrier to fuel is 1.25. The maximum difference between the simulated and experimental results is 0.003 at the outlet where the flow has achieved complete combustion. As indicated by Son and Kim [13], small discrepancies of the outlet gas concentration may exist in the complex chemical reactor such as a CLC unit in the different experimental runs. Fryer and Potter [14] reported that the differences of the outlet concentration between different runs could reach more than 15% when studying the ozone decomposition in a simple bubbling fluidised bed at the same operating conditions. Mattisson *et al.* [15] and Leion *et al.* [15] also pointed out that considerable variations in the outlet concentrations of gaseous species like CH_4, H_2O and CO_2 in the CLC unit during different runs may exist, and the chemical and physical changes of oxygen carriers such as attrition and change in grain size can also contribute to a certain extent differences. Forero *et al.* [2] studied the syngas combustion using the same Cu-based oxygen carrier in the same CLC unit and revealed that the outlet gas concentration in the CLC reactor was diluted by N_2 from the bottom loop seal. However, no error estimates for the outlet gas concentration are provided in their experiments [8], which is hard to help clarifying the real reasons for the difference between the simulation and experimental results. Besides the aforementioned reasons, the discrepancies between the bubble formation frequency and bubble size predicted by the simulation and those of the real experiments can cause the differences in spite of some previously published literatures reporting the reasonable predictions of the hydrodynamic behaviour by employing the similar CFD models [16, 17]. The kinetic model may not be accurate enough to account for the physical and chemical changes of oxygen carriers in the CLC process. As mentioned above, the kinetic model was determined based on TGA experiments and no modification in the kinetic model is made when the ratio of oxygen carrier to fuel is larger than 1.38 based on the trend of the experimental combustion efficiency. It is thus suggested that the proposed kinetic model is used when the ratio of oxygen carrier to fuel is smaller than 1.38.

Characterisation of bubbling using correlations between velocity fluctuation and volume fraction fluctuation

As discussed before, the occurrence of the gas-phase bubble has an influence on the combustion efficiency and the CLC performance. Therefore, controlling the bubble formation and bubble size in the dense bed is a cost-effective approach to improve the efficiency. A parameter correlating the bubble formation and the local dynamic parameters proposed in the previous work [9] has been found to be able to monitor the occurrence of bubbles. We assess its applicability for 3D cylindrical fuel reactor. In order to reflecting the bubble formation behavior more accurately, local area-weighted average dynamic parameters are employed rather than 'point' values as used in 2D model. The area-weighted time correlation for the pressure fluctuation and the local gas-phase velocity fluctuation is expressed in terms of Equation (13). Figure 7 shows the time correlation for $\overline{\boldsymbol{p'v'_g}}$ over the period from 8 to 12s, respectively. Based on Figure 7, the occurrence of the gas-

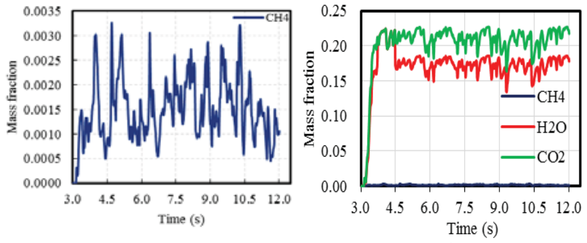

(a) (b)

Figure 5 (a) Time evolution of the mass fraction of a) CH_4; (b) gaseous reactant and products at the outlet of the fuel reactor at 1023K

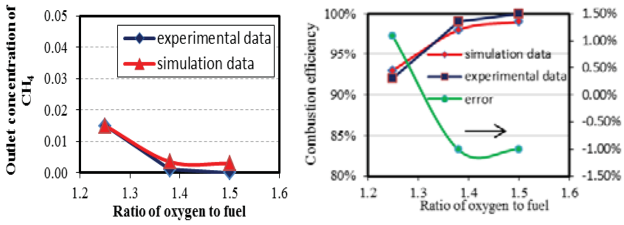

(a) (b)

Figure 6 Comparison of outlet CH_4 concentration at various oxygen carrier to fuel ratio for experiment of Forero *et al.* [8]

$$R(t) = \frac{\overline{p^{'}(t_0, A_{0,} h_0) v_g^{'}(t_0 + \tau, A_{0,} h_0)}}{\sqrt{\overline{p^{'2}(t_0, A_{0,} h_0)}}\sqrt{\overline{v_g^{'2}(t_0, A_0, h_0)}}} \tag{13}$$

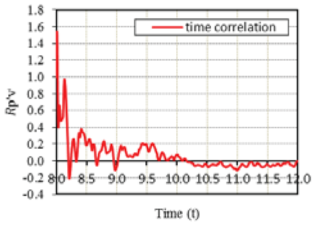

Figure 7 Time-dependent correlation relating the bubble formation of x-y plane cross section with $\overline{p'v'_g}$ at z=0.025 m

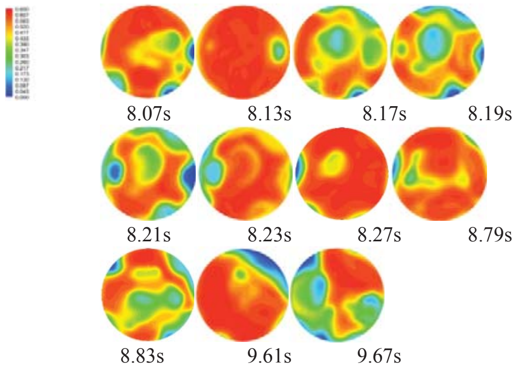

Figure 8 The contour plots of solid phase volume fraction for the validation of time correlation

phase bubble in the position of z=0.025m in the dense bed could be identified because a rapid reduction in the correlation value indicates that the enlargement of a bubble and the reduction of bubble size corresponds to a rapid increase in correlation. This can be clearly seen from Figure 7 that the bubble size in z=0.025m increases during the period of 8.13 to 8.21s, 8.79 to 8.85s while it reduces in the period of 8.07 to 8.13s, 8.23 to 8.27s as indicated by contours shown in Figure 8.

CONCLUSION

In the present study, a CFD Eulerian-Eulerian model was employed to simulate the hydrodynamic behaviour of the flow in a CLC fuel reactor coupled with the heterogeneous reaction. CuO impregnated on Al_2O_3 was used as the oxygen carrier and methane for the gaseous fuel. The main conclusions are:

(1) The salient features of gas-phase bubble in the dense bed of CLC reactor were well captured and traced. It was identified that the formation of fast by-pass gas-phase bubbles in the dense bed has a negative influence on the combustion.
(2) The accuracy of computed outlet concentration of CH_4 was improved with the modified kinetic model. The CFD modelling was validated by comparing the simulation results with the experimental data obtained from the open literature and a good agreement was obtained.
(3) The use of a correlation parameter, which correlates the fluctuations of the local pressure and gas-phase velocities, for characterising the bubble formation has been assessed. The simulation results clearly indicates that this correlation can be used to monitor the variation of bubble at specific position effectively since the bubble formation is highly related with local large eddies in the dense bed.

REFERENCE

1. Adánez, J., P. Gayán, J. Celaya, L.F. de Diego, F. García-Labiano, and A. Abad, *Chemical looping combustion in a 10 kW prototype using a CuOAl2O3 oxygen carrier effect of operating conditions on methane combustion.* Ind. Eng. Chem. Res., 2006. **45**: p. 6075-6080.
2. Forero, C.R., P. Gayán, L.F. de Diego, A. Abad, F. García-Labiano, and J. Adánez, *Syngas combustion in a 500 Wth Chemical-Looping Combustion system using an impregnated Cu-based oxygen carrier.* Fuel Processing Technology, 2009. **90**(12): p. 1471-1479.
3. Deng, Z.G., R. Xiao, B.S. Jin, Q.L. Song, and H. Huang, *Multiphase CFD Modeling for a Chemical Looping Combustion Process (Fuel Reactor).* Chemical Engineering & Technology, 2008. **31**(12): p. 1754-1766.
4. Deng, Z., R. Xiao, B. Jin, and Q. Song, *Numerical simulation of chemical looping combustion process with CaSO4 oxygen carrier.* International Journal of Greenhouse Gas Control, 2009. **3**(4): p. 368-375.
5. Jung, J. and I.K. Gamwo, *Multiphase CFD-based models for chemical looping combustion process: Fuel reactor modeling.* Powder Technology, 2008. **183**(3): p. 401-409.
6. Kruggel-Emden, H., F. Stepanek, and A. Munjiza, *A Study on the Role of Reaction Modeling in Multi-phase CFD-based Simulations of Chemical Looping Combustion.* Oil & Gas Science and Technology – Revue d'IFP Energies nouvelles, 2011. **66**(2): p. 313-331.
7. Harichandan, A.B. and T. Shamim, *CFD analysis of bubble hydrodynamics in a fuel reactor for a hydrogen-fueled chemical looping combustion system.* Energy Conversion and Management, 2014. **86**: p. 1010-1022.
8. Forero, C.R., P. Gayán, F. García-Labiano, L.F. de Diego, A. Abad, and J. Adánez, *High temperature behaviour of a CuO/γAl2O3 oxygen carrier for chemical-looping combustion.* International Journal of Greenhouse Gas Control, 2011. **5**(4): p. 659-667.
9. Chen, L., X. Yang, X. Li, G. Li, and C. Snape, *Prediction of formation of gas-phase bubbles correlated by vortices in the fuel reactor of chemical looping combustion.* Fuel Processing Technology, 2015. **130**: p. 235-244.
10. Abad, A., J. Adánez, F. García-Labiano, L.F. de Diego, and P. Gayán, *Modeling of the chemical-looping combustion of methane using a Cu-based oxygen carrier.* Energy Procedia, 2009. **1**(1): p. 391-398.
11. JOHNSON, P.C. and R. JACKSON, *Frictional-collisional constitutive relation for granular materials with application to plane shearing.* J. Fluid Mech., 1987. **176**: p. 67-93.
12. Adanez, J., A. Abad, F. Garcia-Labiano, P. Gayan, and L.F. de Diego, *Progress in Chemical-Looping Combustion and Reforming technologies.* Progress in Energy and Combustion Science, 2012. **38**(2): p. 215-282.
13. Son, S.R. and S.D. Kim, *Chemical-looping combustion with NiO and Fe2O3 in a thermobalance and circulating fluidized bed reactor with double loops.* Industrial Engineering and Chemical Research, 2006. **45**(8): p. 2689–2696.
14. Mattisson, T., A. Järdnäs, and A. Lyngfelt, *Reactivity of Some Metal Oxides Supported on Alumina with Alternating Methane and OxygenApplication for Chemical-Looping Combustion.* Energy Fuels, 2003. **17**(3): p. 643-651.
15. Leion, H., T. Mattisson, and A. Lyngfelt, *Solid fuels in chemical-looping combustion.* International Journal of Greenhouse Gas Control, 2008. **2**(2): p. 180-193.
16. Guan, Y., J. Chang, K. Zhang, B. Wang, and Q. Sun, *Three-dimensional CFD simulation of hydrodynamics in an interconnected fluidized bed for chemical looping combustion.* Powder Technology, 2014. **268**: p. 316-328.
17. Patil, D.J., M. van Sint Annaland, and J.A.M. Kuipers, *Critical comparison of hydrodynamic models for gas–solid fluidized beds—Part I : bubbling gas–solid fluidized beds operated with a jet.* Chemical Engineering Science, 2005. **60**(1): p. 57-72.

TRANSPORTED JOINT PDF MODELING OF NON-REACTING AND REACTING TURBULENT SPRAY FLOWS

Hu Y., Olguin H.,[1] and Gutheil E.*
*Author for correspondence
Interdisciplinary Center for Scientific Computing,
University of Heidelberg,
Heidelberg, 69120,
Germany,
E-mail: gutheil@iwr.uni-heidelberg.de

ABSTRACT

A hybrid description of the transported joint probability density function (PDF) model and Reynolds-averaged Navier-Stokes (RANS) equations for turbulent poly-disperse non-reacting and reacting spray flows is presented. The $\tilde{k}-\tilde{\varepsilon}$ transport equations with additional spray source terms were solved to provide the turbulent time scales required in the mixing model. The dependent variables of the joint PDFs are the gas velocity and gas the mixture fraction in the non-reacting situation, and the gas mixture fraction and gas enthalpy for spray flames. The transported joint PDF equations are solved with a hybrid finite volume and a Lagrangian Monte Carlo method. Micro mixing is described using the interaction-by-exchange-with-the-mean (IEM) model, and the gas particle velocity is described by the simplified Langevin model, where in both models extra terms to account for spray evaporation are added. For the reacting case, detailed chemistry is considered by means of a spray flamelet model for the ethanol/air system in a counterflow configuration. Simulations of non-reacting acetone/air spray flows and ethanol/air spray flames are carried out. Model predictions of gas temperature, Sauter mean diameter (SMD) as well as mean and fluctuating droplet velocities are discussed in comparison with experimental results from the literature.

NOMENCLATURE

f	[-]	One-point one-time Eulerian probability density function
F	[-]	Mass density function
U	[m/s]	Gas velocity
ω_t	[s^{-1}]	Frequency of turbulent mixing
r_d	[m]	Droplet radius
m_d	[kg]	Droplet mass
T_d	[K]	Droplet temperature
x	[m]	Physical coordinate
C_D	[-]	Drag coefficient
B_M	[-]	Spalding mass transfer number
h	[J/kg]	Total enthalpy
ρ	[kg/m^3]	Density of mass
SMD	[m]	Sauter mean diameter
S_ϕ	[-]	Source term of the variable ϕ

Special characters

Φ	[-]	Characteristic variables in physical space
Ψ	[-]	Characteristic variables in sample space
ξ	[-]	Gas mixture fraction
Γ_t	[kg/m/s]	Turbulent exchange coefficient
ε	[m^2/s^3]	Dissipation rate of the turbulent kinetic energy
δ_{ij}	[-]	Kronecker symbol
χ	[s^{-1}]	Scalar dissipation rate
τ_d	[s]	Droplet relaxation time

Subscripts

g	Gas phase
l	Liquid phase
d	Droplet
t	Turbulent
0	Initial or reference value

INTRODUCTION

Turbulent fuel sprays can be found in many engineering applications such as engine systems for power generation, liquid rocket propulsion and industrial furnaces. Complex physical and chemical phenomena such as turbulent transport, droplet breakup and spray evaporation as well as combustion take place in these devices, which determine their performance. Hence, considerable effort is needed in order to develop suitable models and predictive tools.

The transported probability density function (PDF) method has been used for several decades in numerical studies of turbulent reacting gas flows, and it appears to be a powerful approach for the modeling of a wide range of combustion processes including effects of local extinction, re-ignition and pollution formation [1]. The main advantage of transported PDF methods is that chemical source terms appear in closed form and thus, complex chemical reactions mechanisms can be treated in an exact way. If the transported PDF of the gas velocity is considered, the turbulent convective transport appears in closed form. Thus, the application of transported PDF methods for multiphase flows is very attractive, and it provides a suitable way to capture the local shape of the PDF of variables influenced by the presence of evaporating droplets [2]. Heye et al. [3] used a sub-filter PDF in the large eddy simulation (LES) of a series of methanol spray flames, where auto-ignition processes were studied considering the influence of spray/combustion interactions. For this purpose, the joint scalar PDF transport equations were solved in a Lagrangian framework. Bulat et al. [4] and Jones et al. [5] combined LES

---

[1] Present affiliation: Department of Mechanical Engineering, Universidad Técnica Federico Santa María, Valparaíso, Chile

with a Eulerian-stochastic PDF model, and they applied it to the simulation of an industrial gas-turbine combustion chamber and of a canonical methanol spray flame. Ge and Gutheil [6] derived a joint transported equation of the PDF of the gas mixture fraction and gas enthalpy, and they used it to simulate a turbulent spray flame. In that work, the transported joint PDF approach was coupled with a spray flamelet model [7]. A joint gas phase-composition-frequency-PDF has been applied for the simulation of an evaporating non-reacting spray [8], where the droplet-seen gas velocity was considered.

The workshop series "Measurement and Computation of Turbulent Spray Combustion" (TCS) [9], guided by the aim of advancing the current understanding of basic processes in turbulent spray combustion, was initiated in 2009 and provides benchmark test configurations for both experimentalists and modelers, contributing valuable datasets. In the present study, both non-reacting and reacting spray flows are simulated based on a hybrid RANS/PDF approach for dilute sprays. Two-way coupling of the gas and liquid is considered, and the droplets are tracked in a Lagrangian way. For spray flows, both the momentum and the turbulent mixing in the gas phase are crucial for the spray evolution, and this motivates the choice of a transported joint PDF of the gas velocity and the mixture fraction. In spray flames, gas enthalpy is more important because of the exponential temperature dependence of chemical reaction rates and thus, in this case, a joint gas mixture fraction and gas enthalpy PDF is used. The numerical results are compared with the experimental set B of Gounder et al. [10], which provides measurements for droplet sizes and both the radial and axial velocity components of the droplet size groups.

GAS PHASE

The gas phase is described by a combined RANS/PDF method, where the transported joint PDF of either the gas mixture fraction and gas velocity or the mixture fraction and gas enthalpy are considered, and the remaining variables are closed through the extended κ−ε model with additional terms to account for spray evaporation.

Hybrid RANS/PDF Model

The mass density function $F(\Psi;\mathbf{x},t)$ can be defined in terms of the one-point one-time Eulerian joint PDF $f(\Psi;\mathbf{x},t)$ of multiple fluid properties as $F(\Phi;\mathbf{x},t) = \rho(\Psi)f(\Psi;\mathbf{x},t)$. Then, the joint PDF $f(\Psi;\mathbf{x},t)$ is defined by [11]

$$f(\Psi;\mathbf{x},t) = \langle \delta(\Phi(\mathbf{x},t)-\Psi) \rangle \tag{1}$$

Here, δ is the Kronecker symbol. $\Phi(\mathbf{x},t)$ is the vector of the characteristic variables considered, and Ψ denotes the corresponding variables in sample space. In this study, a joint gas velocity-gas mixture fraction PDF, $\Phi = (U,\xi)$ is used for the non-reacting case, and a joint mixture fraction and gas enthalpy PDF, $\Phi = (\xi,h)$ for the reacting situation is considered. Gas enthalpy becomes dominant in the spray flame because of the exponential temperature dependence of the chemical reaction rates. The mixture fraction of the gas phase is based on the chemical element C [18].

The transport equation of the mass density function $F(\Psi;\mathbf{x},t)$ can be derived as [12,13]

$$\frac{\partial F}{\partial t} + \frac{\partial (U_i F)}{\partial x_i} - \frac{\langle S_\mathrm{v}\rangle}{\langle\rho\rangle}F = -\sum_{\alpha=1}^{N_\alpha}\frac{\partial}{\partial \Psi_\alpha}\left(\left\langle\frac{\mathrm{d}\Phi_\alpha}{\mathrm{d}t}\middle|\Psi\right\rangle F\right) \tag{2}$$

U_i is the Favre-averaged gas velocity, N_α the number of random fluid variables considered, and S_v is the spray source term accounting for spray evaporation. In equation (2), the terms on the left hand side account for changes in the joint PDF due to unsteady effects, transport in physical space, and spray evaporation. The terms on the right-hand side correspond to the probability transport in sample space, where terms concerning molecular diffusion and velocity fluctuations depend on multi-point information. Making use of the governing equations of gas velocity, gas mixture fraction and gas enthalpy, and after closure of terms associated with molecular transport, equation (2) can be rewritten in its final form [14, 15].

Due to the high dimensionality of the joint PDF transport equation, traditional finite difference schemes are not suitable to solve this equation. A Lagrangian Monte-Carlo method has been introduced by Pope [16] to overcome this situation. This method treats the continuous gas flows in terms of a large number of discrete notional gas particles, where each particle attains the properties, (m^*,x^*,U^*,ξ^*) for the joint velocity-mixture fraction PDF and (m^*,x^*,ξ^*,h^*) for the joint PDF of mixture fraction and enthalpy. The joint PDF transport equation can then be transformed into a set of stochastic differential equations (SDEs), which provides the basic evolution of each particle's properties. When a joint mixture fraction-enthalpy PDF is considered, this evolution involves the equations for the position of each particle x^*, mixture fraction ξ^*, and enthalpy h^*,

$$\begin{aligned}
\mathrm{d}x_i^* &= \left(\tilde{U}_i + \frac{1}{\langle\rho\rangle}\frac{\partial \Gamma_\mathrm{t}}{\partial x_i}\right)\mathrm{d}t + \left(\frac{2}{\langle\rho\rangle}\Gamma_\mathrm{t}\right)^{1/2}\mathrm{d}W_i \\
\mathrm{d}\xi^* &= \left(-\frac{1}{2}\omega_\mathrm{t}(\xi^* - \langle\xi\rangle) + (1-\langle\xi\rangle)\frac{\langle S_\mathrm{v}\rangle}{\langle\rho\rangle}\right)\mathrm{d}t \\
\mathrm{d}h^* &= \left(-\frac{1}{2}\omega_\mathrm{t}(h^* - \langle h\rangle) + (\langle S_\mathrm{e}\rangle - \langle h\rangle\langle S_\mathrm{v}\rangle)\frac{1}{\langle\rho\rangle}\right)\mathrm{d}t
\end{aligned} \tag{3}$$

where $\Gamma_\mathrm{t} = \mu_\mathrm{t}/\mathrm{Sc}_\mathrm{t}$ is the turbulent transport coefficient and μ_t denotes the turbulent viscosity and Sc_t is the turbulent Schmidt number. $\mathrm{d}W_\mathrm{i}$ is the increment of a stochastic Wiener process, which is determined from a Gaussian random number generator with mean $\langle \mathrm{d}W_i(t)\rangle=0$ and covariance $\langle \mathrm{d}W_i(t)\mathrm{d}W_j(t)\rangle = \mathrm{d}t\delta_{ij}$. $\omega_\mathrm{t} = \tilde{\varepsilon}/\tilde{k}$ is the frequency of turbulent mixing, where $\tilde{k}$ and $\tilde{\varepsilon}$ are the turbulent kinetic energy and its dissipation rate, respectively. With the joint gas velocity-mixture fraction PDF, a gas particle velocity equation is also solved in terms of the extended simplified Langevin model [17]

$$\begin{aligned}
\mathrm{d}U_i^*(t) = &\left(g_i - \frac{1}{\langle\rho\rangle}\frac{\partial\langle p\rangle}{\partial x_i} + \frac{1}{\langle\rho\rangle}(\langle S_{\mathrm{m},i}\rangle - \langle U_i\rangle\langle S_\mathrm{v}\rangle)\right)\mathrm{d}t \\
&- \left(\frac{1}{2} + \frac{3}{4}C_0\right)(U_i^*(t) - \langle U_i\rangle)\omega_\mathrm{t}\mathrm{d}t + \sqrt{C_0\tilde{\varepsilon}}\,\mathrm{d}W_i
\end{aligned} \tag{4}$$

Here, the spray source terms are added to the drift term, which represents the force exerted by the droplets on the gas. $S_{\mathrm{m},i}$ is the interphase momentum source term. For the closure of the

PDF transport equation, the Favre-averaged transport equations of mass, momentum and enthalpy of the gas phase are solved together with extended $\tilde{k}-\tilde{\varepsilon}$ equations in the turbulent spray flow. The general form of the gas phase Favre-averaged transport equations is written as

$$\frac{\partial(\langle\rho\rangle\tilde{\phi})}{\partial t}+\frac{\partial(\langle\rho\rangle\tilde{U}_j\tilde{\phi})}{\partial x_j}-\frac{\partial}{\partial x_j}\left(\Gamma_{\tilde{\phi},\mathrm{eff}}\frac{\partial\tilde{\phi}}{\partial x_j}\right)=S_{g,\phi}+S_{l,\phi} \qquad (5)$$

$S_{g,\phi}$ denotes the gas phase source term [18], and $S_{l,\phi}$ is the liquid phase source term for the conserved variables $\tilde{\phi}$.

Spray Flamelet Model

The spray flamelet model is used for the inclusion of detailed chemistry [19]. This model is able to capture evaporation effects on the structure of laminar flamelets. The generation of the spray flamelet library is achieved by the pre-calculation of a ethanol/air counterflow spray flame with consideration of a detailed chemical reaction mechanism consisting of 38 species and 337 elementary reactions [7]. The Favre-averaged mean values of the scalars, $\tilde{\Phi}$, are obtained as [19]

$$\tilde{\Phi}=\int_0^\infty\int_{-\infty}^\infty\int_0^\infty\int_0^\infty\int_0^1\Phi\tilde{f}(\xi,\chi,E,R_0,v_0)d\xi_C d\chi dE dR_0 dv_0 \qquad (6)$$

R_0 and v_0 denote the initial droplet radius and velocity, respectively, and E the global equivalence ratio at the spray inlet. f denotes the joint probability density function of the considered characteristic variables. Statistical independence of the different variables is assumed, and a Dirac-delta function is used to describe the initial droplet velocity, droplet size, and equivalence ratio. The scalar dissipation rate is modeled through a log-normal distribution, whereas the mixture fraction is assumed to follow a β-distribution. Since Ge and Gutheil [2] showed that the standard presumed β distribution is not adequate for representing the mixture fraction in spray flows. For this reason, in the present study, the PDF of mixture fraction obtained from the joint PDF transport equation is used.

LIQUID PHASE

A dilute spray is assumed, droplet-droplet interactions are neglected, and droplets are assumed to be spherically symmetric. Thus, the droplet velocity, $\mathbf{V}_\mathrm{d}$ is computed considering the influence of drag force and gravity

$$\frac{\mathrm{d}\mathbf{V}_\mathrm{d}}{\mathrm{d}t}=\frac{3}{8}\frac{1}{r_\mathrm{d}}\frac{\rho_\mathrm{g}}{\rho_l}C_D(\mathbf{U}-\mathbf{V}_\mathrm{d})|\mathbf{U}-\mathbf{V}_\mathrm{d}|+\mathbf{g} \qquad (7)$$

Here, $\mathbf{g}$ is the gravitational acceleration. The drag coefficient C_D depends on the droplet Reynolds number, and it is determined by the Schiller-Naumann correlation. μ_g is the gas viscosity and ρ_g the density of the gas mixture. The subscript 'g' denotes the gas phase and 'd' refers to the droplets. The mass of a droplet with radius r_d is $m_\mathrm{d} = 4/3\pi r_\mathrm{d}^3\rho_\mathrm{l}$. The Abramzon-Sirignano model [20] is used for the calculation of the mass evaporation rate

$$-\frac{\mathrm{d}m_\mathrm{d}}{\mathrm{d}t}=\dot{m}_\mathrm{d}=2\pi r_\mathrm{d}\hat{\rho}\hat{D}\widetilde{\mathrm{Sh}}\ln(1+\mathrm{B_M}) \qquad (8)$$

with $\mathrm{B_M} = (Y_\mathrm{s} - Y_\infty)/(1 - Y_\mathrm{s})$, where Y_s and Y_∞ describe the mass fraction of vapor fuel at the droplet surface and in the local ambient gas phase, respectively. Assuming a uniform temperature distribution within the droplet, an infinite conductivity model including non-equilibrium effects at the droplet surface is considered [21]

$$\frac{\mathrm{d}T_\mathrm{d}}{\mathrm{d}t}=\frac{f_2\widetilde{\mathrm{Nu}}}{3\mathrm{Pr_g}}\frac{1}{\tau_\mathrm{d}}\left(\frac{C_{pg}}{C_{pl}}\right)(T_\mathrm{g}-T_\mathrm{d})-\frac{L_V(T_\mathrm{d})}{C_{pl}}\left(\frac{\dot{m}_\mathrm{d}}{m_\mathrm{d}}\right) \qquad (9)$$

where $\tau_\mathrm{d} = 2/9\rho_\mathrm{l}r_\mathrm{d}^2/\mu_\mathrm{g}$ is the droplet relaxation time. C_{pg} and $C_{p\mathrm{l}}$ are the heat capacity of gas and liquid phase, respectively, and $L_V(T_\mathrm{d})$ is the temperature dependent latent heat of vaporization. f_2 is a correction factor introduced for taking into account the heat transfer due to evaporation. Convective droplet evaporation is considered through use of the modified Nusselt $\widetilde{\mathrm{Nu}}$ and Sherwood $\widetilde{\mathrm{Sh}}$ numbers, see equations (8) and (9) [20]. The spray source terms S_v, S_m, and S_e appearing in equations (3)-(4) account for the liquid and gas coupling through interphase exchanges of mass, momentum and energy [2]

$$\begin{aligned}S_\mathrm{v}&=\sum^{n_\mathrm{d}}N_{\mathrm{d},k}\dot{m}_\mathrm{d}\\S_\mathrm{m}&=\sum_{k=1}^{n_\mathrm{d}}N_{\mathrm{d},k}\left[-m_\mathrm{d}\frac{\mathrm{d}\mathbf{V}_{\mathrm{d},k}}{\mathrm{d}t}+\dot{m}_\mathrm{d}\mathbf{V}_{\mathrm{d},k}\right]\\S_\mathrm{e}&=\sum_{k=1}^{n_\mathrm{d}}N_{\mathrm{d},k}\left[-\frac{\mathrm{d}}{\mathrm{d}t}(m_\mathrm{d}C_{pl}T_\mathrm{d})-\frac{1}{2}\frac{\mathrm{d}}{\mathrm{d}t}(m_\mathrm{d}\mathbf{V}^2_{\mathrm{d},k})\right]\end{aligned} \qquad (10)$$

Here, n_d is the total number of computational droplet parcels that pass through the considered grid cell, and $N_{\mathrm{d,k}}$ is the number of droplets bore by each computational parcel k [18].

TEST CASES

In the present study, three poly-disperse turbulent acetone spray flows (SP2, SP6, and SP7) in air and one dilute ethanol/air pray flame, EtF6, from the Sydney database [10] are considered. The spray burner is composed of a central jet nozzle with diameter D = 10.5 mm and a surrounding co-flow air stream with a diameter of 104 mm. This co-flow burner is mounted in a wind tunnel with bulk velocity of 4.5 m/s. For the reactive case EtF6, a hot pilot jet flame with diameter 25 mm is supplied around the central fuel jet to stabilize the main flame. The flow rates of different streams at the inlet boundary for the four cases considered in this paper are listed in Tab. 1.

Table 1 Inflow conditions of the acetone sprays SP2, SP6, and SP7; ethanol spray flame EtF6, set B, taken from [10].

Parameter	SP2	SP6	SP7	EtF6
Bulk jet velocity (m/s)	36	36	60	36
Carrier mass flow rate (g/min)	225	225	376	225
Liq. fuel injection rate (g/min)	75	45	75	45
Liq. fuel rate at inlet (g/min)	33.9	26.7	44.2	41.1
Vapor fuel rate at inlet (g/min)	41.0	18.3	30.8	3.9

NUMERICAL SOLUTION PROCEDURE

In this work, simulations were carried out using an in-house code with a consistent Eulerian-Lagrangian-Lagrangian formulation for the description of the continuous gas and the dispersed liquid phase. A two-dimensional axisymmetric computational domain extending to 40*D* and 13.8*D* in the axial and radial direction, respectively, was employed, the sketch of which is given in Figure 1. The solution of the gas phase PDF is achieved by numerical integration of the SDEs (3)-(4) for notional gas particles. At every time step, new gas particles are supplied at the inlet, and they are removed from the ensemble if they have moved out of the computational domain. The number of the gas particles per cell is initially prescribed to be 50, and a particle number control algorithm is included to maintain the number of particle around this value [2]. The Favre-averaged mean variables appearing in the PDF model are computed with a Eulerian finite-volume method. The governing equation (5) is discretized over the staggered grid and solved by a two-dimensional finite-volume CFD solver, where the SIMPLE algorithm is employed to couple the velocity and pressure field. For the ethanol/air [7] spray flame, the spray flamelet model [18] is included.

RESULTS AND DISCUSSION

In this section, the computed results will be presented and compared with experimental data set B of Gounder et al. [10].

Acetone Spray Flows

Figure 2 shows the contour plot of the mean gas mixture fraction computed for spray SP6, in which the filled dots show the distribution of representative droplets in the gas flow. Since in non-reacting cases the mixture fraction has a linear relation with the local mass fraction of vapor fuel, Figure 2 implies a high concentration of fuel vapor near to the fuel inlet, which retards the evaporation process in this region. The four monitor positions A, B, C, and D are selected for the local analysis of the joint PDFs, which will be discussed below.

The droplet size distribution may be characterized by its Sauter mean diameter (SMD). The computed SMD for the three spray flows under consideration are compared with experimental data at the cross-sections *x/D* = 5 and 20, see Figure 3. Generally, good agreement of numerical and experimental results is observed, especially at *x/D* = 5. In terms of the experimental data, the profile of the SMD of SP7 differs from the other two cases, which indicates that the carrier gas velocity or the inlet turbulence level have a stronger effect on the droplet size distribution than the inflow liquid mass loading.

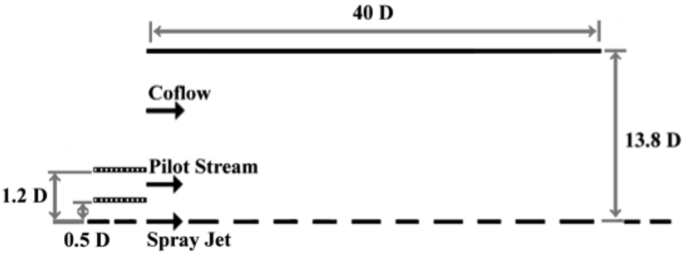

Figure 1 Sketch of the computational domain

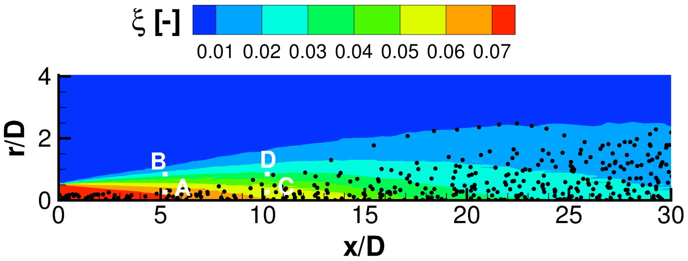

Figure 2 Contour plot of the mean mixture fraction for case SP6 and monitor positions for the analysis of the joint PDF.

The radial mean velocity and mean velocity fluctuation profiles at *x/D* = 5, for the droplet size group $0 < d_d \leqslant 10$ μm, are shown in Figure 4. Significant discrepancies between numerical results and experimental data are found for the fluctuating droplet velocity. In spray flow SP7, the absolute value of the velocity fluctuation is higher than for the other two cases, and differences between computed and measured values become more evident. The small droplets, due to their small Stokes number, are usually treated as tracer particles in the gas flow field, and thus, the deviation in fluctuating velocity prediction implies that the turbulence level is underestimated in the present simulation.

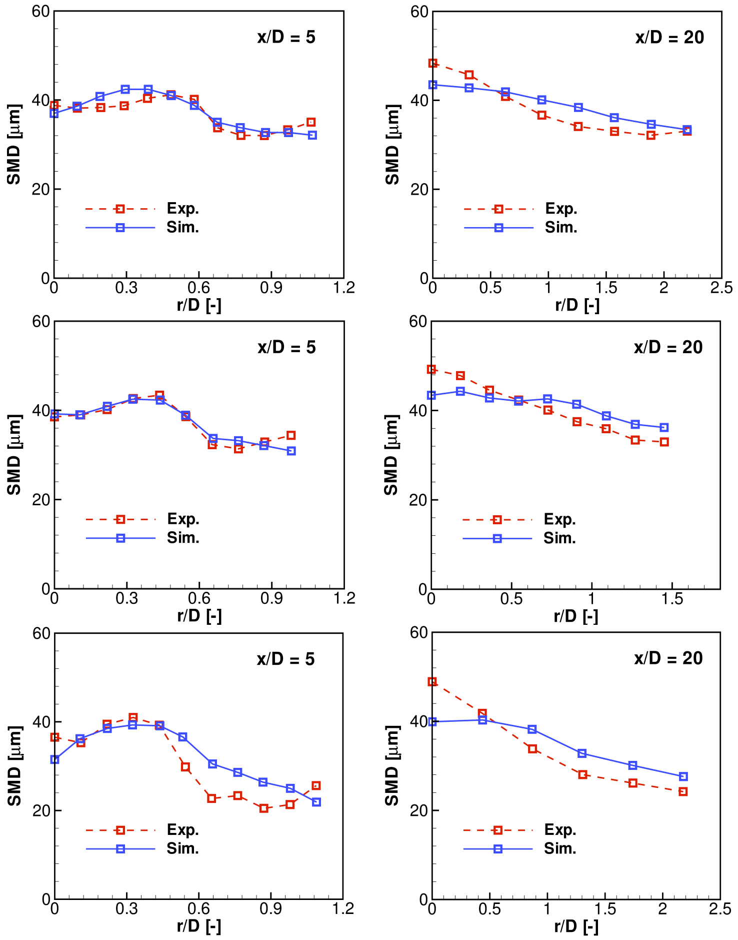

Figure 3 Radial profiles of the Sauter mean diameter. SP2 (top), SP6 (center) and SP7 (bottom).

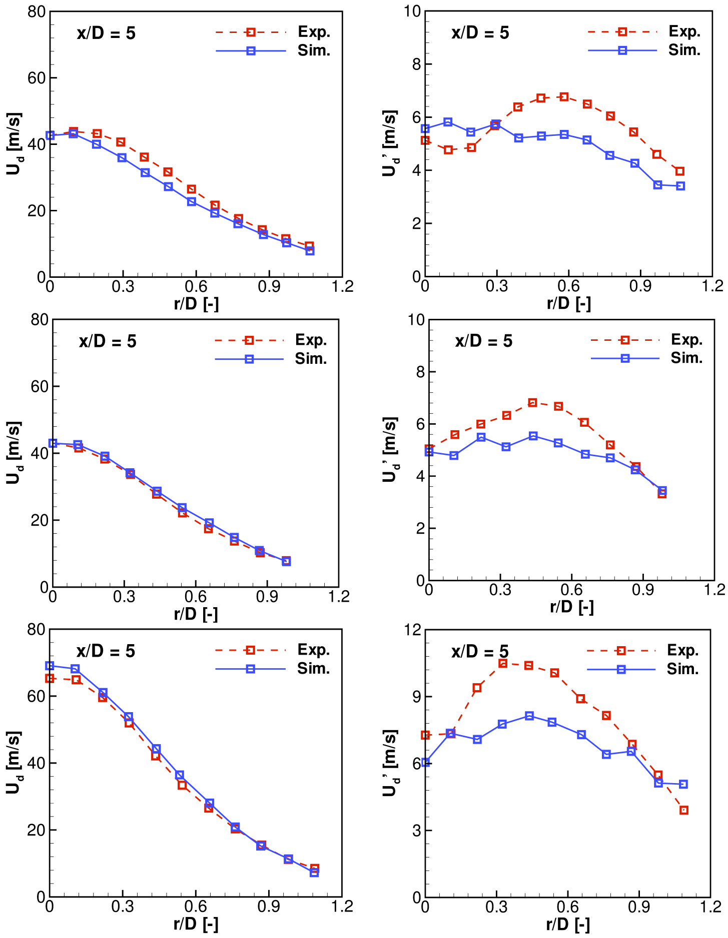

Figure 4 Radial profiles of the droplet mean axial velocity (left) and its fluctuating velocity (right) for droplet size group $0 < d_d \leqslant 10$ µm. SP2 (top), SP6 (center) and SP7 (bottom).

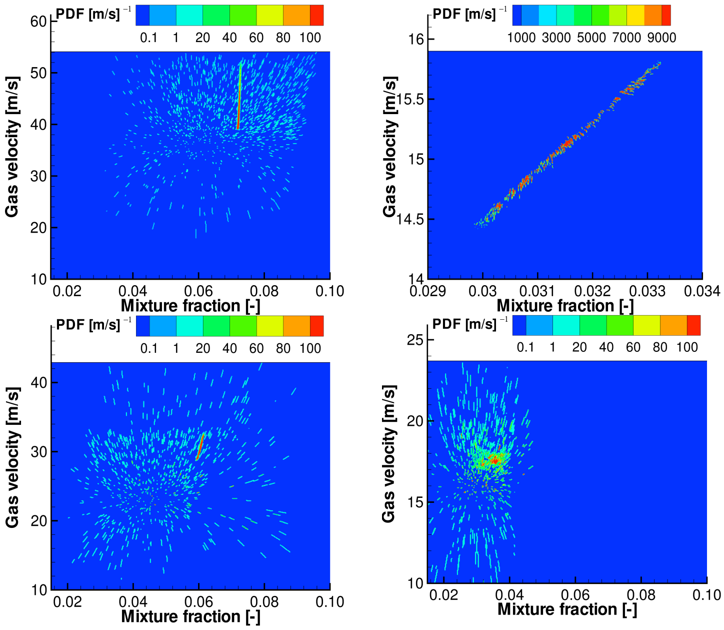

Figure 5 Joint PDF of the gas velocity and the gas mixture fraction at the four selected monitor positions, cf. Fig. 2.

Figure 5 displays the joint PDF of the gas velocity and the mixture fraction calculated at the four selected monitor points A, B, C, and D, cf. Fig. 2, where A refers to the top left, B to the top right, C to the bottom left and D to the bottom right part of the figure. A linear dependence is observed at position B. Due to the dominant effect of turbulent convection near the centerline, correlations between gas velocity and mixture fraction are more similar to each other at positions A and C than at B and D.

Ethanol Spray Flame

Figure 6 shows the comparison of computed and measured gas temperature at *x/D* = 10, 20, and 30. Numerical results generally follow the trend of experimental data, although over-predictions are found at some locations. The simulation of this flame with LES [22] shows similar deviation of the computed gas temperature at cross-section *x/D* = 10, and it was argued that the pilot flame might be part of the reason for the discrepancies.

Figures 7 and 8 show the radial profiles of the SMD and the mean and fluctuating droplet velocities for both numerical and experimental results. Reasonable agreement is obtained. However, the SMD close to the nozzle exit is somewhat higher than the experimental data due to the over-prediction of the gas temperature, leading to enhanced evaporation. The radial distribution of droplet mean axial velocity matches the trend observed in the experiments. The radial distribution of droplet mean axial velocity matches the trend observed in the experiments. At *x/D* = 20, the droplet velocity fluctuations become higher than those at *x/D* = 5, showing an expanding turbulent shear layer downstream, which is not captured by the simulations.

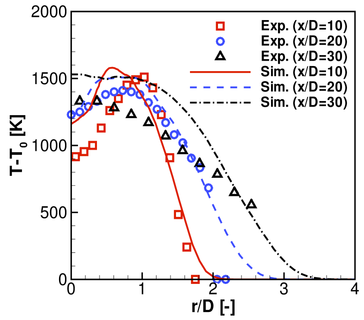

Figure 6 Radial profiles of mean excess gas temperature at *x/D*= 10, 20 and 30 for the ethanol spray flame (EtF6).

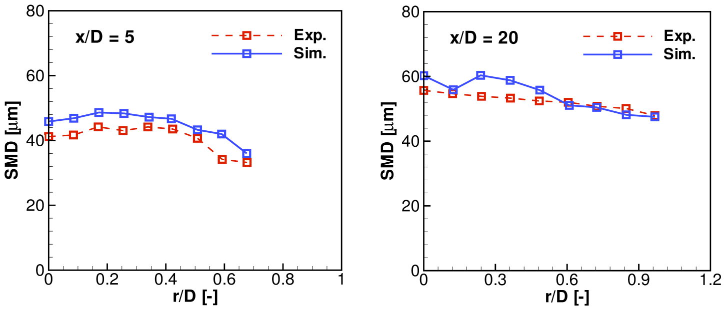

Figure 7 Radial profiles of the Sauter mean diameter (EtF6).

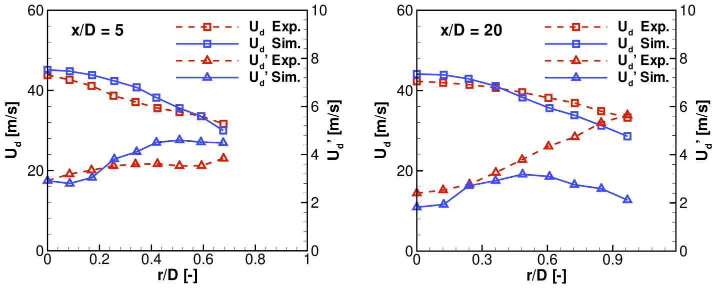

Figure 8 Radial profiles of the axial mean and the fluctuating droplet velocities (EtF6).

This increase in the profile of the fluctuating droplet velocity may be attributed to the effect of thermal expansion in combustion processes, and more sophisticated droplet dispersion models are expected to improve the present predictions [22].

CONCLUSION

A two-dimensional transported joint PDF model is used to simulate turbulent non-reacting and reacting spray flows. Three different poly-disperse turbulent acetone spray flows in air with different inlet mass loadings and turbulence levels, and one turbulent ethanol/air spray flame are considered. For all cases under investigation, experimental data [10] are available for comparison with the simulations. For the non-reactive case, numerical results generally show a good agreement with measurements in terms of droplet size and mean droplet velocity, but some discrepancies are observed for the droplet fluctuating velocities. The analysis of the joint PDFs shows that a linear correlation between gas velocity and mixture fraction is found close to the nozzle exit, and no regions are found where statistical independence prevails. In the reacting sprays, the computed droplet Sauter mean diameter displays a higher value than the experimental values near the nozzle exit of the spray. This may be associated with the overestimation of the gas temperature near the centerline and in regions close to the nozzle exit, which may be associated with the pilot flame used in the experiment for flame stabilization. More sophisticated turbulence models or droplet dispersion models as well as an improved consideration of the pilot flame are expected to improve the numerical simulations.

ACKNOWLEDGMENT

The authors thank A.R. Masri, Sydney University, Australia for providing the experimental data. Financial support from CSC and Graduate school "MathComp" is gratefully acknowledged.

REFERENCES

[1] Haworth, D., Progress in probability density function methods for turbulent reacting flows, *Progress in Energy and Combustion Science*, Vol. 36, 2010, pp. 168 – 259

[2] Ge, H.-W., and Gutheil, E., Probability density function (PDF) simulation of turbulent spray flows, *Atomization and Sprays*, Vol. 16, 2006, pp. 531–542

[3] Heye, C., Raman, V., and Masri, A.R., Influence of spray/ combustion interactions on auto-ignition of methanol spray flames. *Proceedings of the Combustion Institute*, Vol. 35, 2015, pp. 1639 – 1648

[4] Bulat, G., Jones, W., and Marquis, A., NO and CO formation in an industrial gas-turbine combustion chamber using LES with the Eulerian sub-grid PDF method, *Combustion and Flame*, Vol. 161, 2014, pp. 1804 – 1825

[5] Jones, W., Marquis, A., and Noh, D., LES of a methanol spray flame with a stochastic sub-grid model, *Proceedings of the Combustion Institute*, Vol. 35, 2015, pp. 1685 – 1691

[6] Ge, H.-W., and Gutheil, E., Simulation of a turbulent spray flame using coupled PDF gas phase and spray flamelet modeling, *Combustion and Flame*, Vol. 153, 2008, pp. 173 – 185

[7] Gutheil, E., Structure and extinction of laminar ethanol-air spray flames, *Combustion Theory and Modelling*, Vol. 5, 2001, pp. 131–145

[8] Anand, G., and Jenny, P., Stochastic modeling of evaporating sprays within a consistent hybrid joint PDF framework, *Journal Computational Physics*, Vol. 228, 2009, pp. 2063– 2081

[9] Gutheil, E., Masri, A., Mastorakos, E., Merci, B., Raman, V., Roekaerts, D., and Sadiki, A., TCS, 2015. http://www.tcs-workshop.org/

[10] Gounder, J. D., Kourmatzis, A., and Masri, A.R., Turbulent piloted dilute spray flames: flow fields and droplet dynamics, *Combustion and Flame*, Vol. 159, 2012, pp. 3372 – 3397

[11] Pope S.B., Turbulent flows. Cambridge, UK: Cambridge University Press; 2000.

[12] Humza, R.M., Hu, Y., and Gutheil, E., Probability density function modeling of turbulent spray combustion, In *Experiments and Numerical Simulations of Diluted Sprays*, B. Merci and E. Gutheil, eds., Springer, Heidelberg, 2014.

[13] Pope, S.B., PDF methods for turbulent reactive flows, *Progress in Energy and Combustion Science*, Vol. 11, 1985, pp. 119 – 192

[14] Ge, H.-W., Hu, Y., and Gutheil, E., Joint gas-phase velocity scalar PDF modeling for turbulent evaporating spray flows, *Combustion Science and Technology*, Vol. 184, 2012, pp. 1664–1679

[15] Ge, H.-W., Düwel, I., Kronemayer H., Dibble R. W., Gutheil, E., Schulz C., and Wolfrum J., Laser-Based Experimental and Monte Carlo PDF Numerical Investigation of an Ethanol/Air Spray Flame, *Combustion Science and Technology*, Vol. 180, 2008, pp. 1529–1547

[16] Pope, S.B., A Monte Carlo Method for the PDF Equations of Turbulent Reactive Flow, *Combustion Science and Technology*, Vol. 25, 1981, pp. 159–174

[17] Hu, Y., and Gutheil, E., Transported Joint PDF Modeling of Dilute Turbulent Spray Flows, *Europe 2014, 26th Annual Conference on Liquid Atomization and Spray Systems*, Bremen, Germany, Sep. 2014.

[18] Hollmann, C., Gutheil, E., Modeling of turbulent spray diffusion flames including detailed chemistry, *Proceedings of the Combustion Institute*, Vol. 26, 1996, pp. 175–192

[19] Hollmann, C., Gutheil, E., Flamelet modeling of turbulent spray diffusion flames based on a laminar spray flame library, *Combustion Science and Technology*, Vol. 135, 1998, pp. 1731–1738

[20] Abramzon, B., and Sirignano, W., Droplet vaporization model for spray combustion calculations, *International Journal of Heat and Mass Transfer*, Vol. 32, 1989, pp. 1605 – 1618

[21] Miller, R., Harstad, K., and Bellan, J., Evaluation of equilibrium and non-equilibrium evaporation models for many-droplet gas-liquid flow simulations, *International Journal of Multiphase Flow*, Vol. 24, 1998

[22] De, S., and Kim, S. H., Large eddy simulation of dilute reacting sprays: droplet evaporation and scalar mixing, *Combustion and Flame*, Vol. 160, 2013, pp. 2048 – 2066

TOWARDS A UNIVERSAL DIMENSIONLESS MAP OF FLOW REGIME TRANSITIONS IN HORIZONTAL LIQUID-LIQUID FLOWS

Ibarra R.*, Zadrazil I., Markides C.N. and Matar O.K.
*Author for correspondence
Department of Chemical Engineering,
Imperial College London,
London, SW7 2AZ,
United Kingdom,
E-mail: r.ibarra-hernandez13@imperial.ac.uk

ABSTRACT

The characterisation of co-current horizontal liquid-liquid pipe flow is commonly carried out through experimental investigations in laboratory conditions, which are used to reveal the geometrical features (i.e., spatial distributions) of the two immiscible liquid phases flowing in the pipe. This information is then used to classify the resulting flows into distinct regimes, such as stratified, intermittent and dispersed flow, with very different characteristics. The vast majority of flow regime maps have been compiled based on the (dimensional) mixture or superficial flow velocities of the two phases. This limits the applicability and transferability of these flow regime maps since the maps obtained are a unique representation of the specific flow under investigation. In this paper, newly acquired experimental data together with data available from the literature are used to analyse the conditions that are associated with flow transitions in horizontal liquid-liquid flows. The present experimental study was performed in an 8.5 m long horizontal acrylic pipe of 32-mm internal diameter, using an aliphatic oil (Exxsol D140) and water as the test fluids. A dimensional analysis is carried out to describe the flow regime transitions in a dimensionless flow regime map that represent the governing forces in the flow: inertial, viscous, gravitational (buoyancy) and capillary forces (interfacial tension). The constructed dimensionless flow regime transitions map, based on experimental data, enables the identification of flow regimes in horizontal pipes for different flow velocities, fluid properties and pipe sizes.

INTRODUCTION

The co-current flow of two immiscible liquids in a pipe is relevant to many diverse applications across a range of scales, from microfluidic mixers and reactors to transportation pipelines in the oil-and-gas industry. In particular, a number of studies have been carried out to characterise oil-water flows in horizontal pipes, such as, Russell *et al.* [1], Charles *et al.* [2], Oglesby [3], and Trallero [4]. These studies have developed flow regime maps as functions of dimensional variables (i.e. mixture or superficial velocities). As a result, flow regime transitions are unique to each study and cannot be transferred and applied reliably to characterise flows of different fluids, or at different geometrical scales and flow conditions (i.e. pipe sizes, fluid properties, flow rates).

Dimensional analysis can be employed to assist with the improved characterisation of these flows by providing dimensionless descriptions of the important/controlling independent variables. Based on these dimensionless variables, improved flow regime maps can be proposed that collapse information across scales, fluids and conditions.

Scale-up or scale-down can only be performed if similarity exists between a model flow and the actual flow of interest. This similarity comprises three main aspects: geometric similarity, kinematic similarity and dynamic similarity. Geometric similarity concerns the reproduction of all flow/phase length-scale ratios; kinematic similarity concerns ratios of velocities; and dynamic similarity relates ratios between the forces acting on the flow.

NOMENCLATURE

A	[m^2]	Cross-sectional pipe area
D	[m]	Inside pipe diameter
Eo	[-]	Eotvös number
Fr	[-]	Froude number
g	[m/s^2]	Gravitational acceleration
L	[m]	Length
Q	[m^3/s]	Volumetric flow rate
Re	[-]	Reynolds number
U	[m/s]	Velocity
We	[-]	Weber number
WC	[-]	Water cut

Special characters

α	[-]	Wettability
ε	[m]	Pipe roughness
λ	[-]	Non-slip liquid holdup
μ	[Pa.s]	Viscosity
ρ	[kg/m^3]	Density
γ	[N/m]	Interfacial tension

Subscripts

L	Liquid
m	Mixture
o	Oil phase
so	Superficial oil
sw	Superficial water
T	Total
w	Water phase

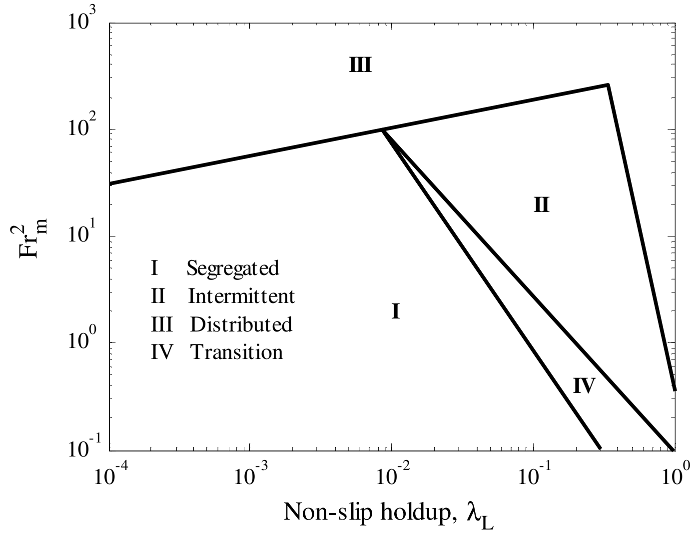

Figure 1 Gas-liquid dimensionless flow regime map for horizontal pipes (adapted from Beggs and Brill [6])

Dimensionless parameters have been used previously in the literature to generalise the regime map of gas-liquid flows in pipes (see, for example, Baker [5], Beggs and Brill [6] or Weisman and Kang [7]). These dimensionless flow regime maps, in which transitions are constructed from experimental data, have proven to be relatively reliable for a given set of conditions. The extension of these maps to different conditions required further analysis because the flow instabilities that result in regime transitions are governed by specific combinations of fluid properties, pipe sizes and flow velocities [8]. Transitions to dispersed flows can be characterised by the Reynolds number while instabilities at the interface by the Weber number. Beggs and Brill [6] developed a dimensionless flow regime map as a function of the non-slip liquid holdup λ_L and the mixture Froude number $Fr_m = U_m/\sqrt{gD}$, as shown in Figure 1. Beggs and Brill [6] performed experiments using air and water in pipes with diameters between 1 and 1.5 in. As a result, the effect of fluid properties was not included in their dimensionless flow regime map. Nevertheless, acceptable results were obtained over a wide range of oil properties mainly attributed to the consistent behaviour of gas-liquid flows in pipes where flow regime transitions are well defined.

This is expected to differ from liquid-liquid flows, where the complex hydrodynamic behaviour makes the regime characterisation a more challenging task due to the additional parameters (and effects) in the system, such as, interfacial phenomena, pipe wettability, and phase inversion.

The purpose of this present study is to develop a dimensionless flow regime map with which to characterise the transitions of liquid-liquid flows in horizontal pipes. Experimentally acquired data are compared with information from previous studies as reported in the literature. The data are used to compile a universal flow regime map for the transitions between stratified flow, dual continuous, dispersion of oil in water with a water layer and dispersed flows.

DIMENSIONAL ANALYSIS OF LIQUID-LIQUID FLOWS

Dimensional analysis is based on the determination of the dimensionless variable groups that describe a flow system. Dimensionless groups can be identified either by empirical or by fundamental considerations. Empirically, dimensionless groups can be identified from the analysis of experimental data acquired for a specific set of conditions. Dimensional groups based on fundamental considerations take into account the governing equations of the flow system (mass, momentum, energy), therefore providing information on the relative magnitude of the normalised terms in these equations [9].

Dimensionless groups can be obtained from the implementation of the Buckingham Π theorem, based on the knowledge of the independent system variables and the fundamental dimensions. In liquid-liquid flow systems, a significant number of independent variables are encountered due to the presence of two phases flowing in the same pipe. Specifically, for fully develop, steady-state and isothermal flow in horizontal pipes, eleven relevant independent variables are obtained, which are the: oil superficial velocity (U_{so}), water superficial velocity (U_{sw}), oil density (ρ_o), water density (ρ_w), oil viscosity (μ_o), water viscosity (μ_w), interfacial tension (γ), inside pipe diameter (D), pipe roughness (ε), wettability (α), and gravitational acceleration (g). In addition, assuming isothermal flow, three fundamental dimensions are selected, namely: mass, length and time.

Dimensional analysis utilises the independent system variables and fundamental dimensions to obtain the dimensionless groups that fully define the flow problem and which can be used to relate full-scale to model flows. Based on the Buckingham Π theorem, the number of dimensionless groups is equal to the number of system variables minus the fundamental dimensions. As a result, eight dimensionless groups are expected that can describe the physical phenomena in liquid-liquid flows. In this study, the dimensionless groups that are listed in Table 1 below have been selected.

Table 1 Dimensionless groups in horizontal liquid-liquid flow

No.	Dimensionless groups	
1	Wettability	α
2	Relative roughness	ε/D
3	Density ratio	$\tilde{\rho} = \rho_o/\rho_w$
4	Viscosity ratio	$\tilde{\mu} = \mu_o/\mu_w$
5	Water cut	$WC = \frac{U_{sw}}{U_{so} + U_{sw}}$
6	Mixture Reynolds number	$Re_m = \frac{\rho_m U_m D}{\mu_m}$
7	Eotvös number	$Eo = \frac{(\rho_w - \rho_o) g D^2}{\gamma}$
8	Mixture Froude number	$Fr_m = \frac{U_m}{\sqrt{gD}}$

In Table 1, the mixture velocity U_{m} is defined as the total volumetric flow rate divided by the cross-section area of the pipe, $U_{\mathrm{m}} = Q_{\mathrm{T}}/A$. In addition, the mixture density and viscosity are averaged based on the volumetric phase fractions assuming no-slip conditions (Dukler *et al.* [10]):

$$\rho_{\mathrm{m}} = \rho_{\mathrm{w}} WC + \rho_{\mathrm{o}}(1 - WC) \quad (1)$$

$$\mu_{\mathrm{m}} = \mu_{\mathrm{w}} WC + \mu_{\mathrm{o}}(1 - WC) \quad (2)$$

EXPERIMENTAL METHODS

The experimental data were acquired in the Two-Phase Oil-Water Experimental Rig (TOWER), shown in Figure 2. The flow facility consists of a 32-mm internal diameter horizontal test section made of acrylic with a total length of 8.5 m. The test fluids were water and an aliphatic oil (Exxsol D140). Table 2 shows the physical properties of the test fluids.

The two phases were circulated by using pumps with a maximum capacity of 160 L/min each. The volumetric flow rates of each phase were measured by two NB liquid turbine flowmeters installed in each line, with capacities of 2-20 L/min and 14-140 L/min, and an accuracy of ±0.5% of full scale. The fluids were introduced into the test section by a T-junction with a horizontal plate to separate the fluids, as shown in Figure 3. The oil phase was introduced from the top of the channel while the water phase from the bottom of the channel. A set of two meshes and one flow straightener were installed in the inlet section to reduce secondary flows and turbulent eddies, and to make the velocity profile more uniform. Table 3 shows the inlet configurations used in the experimental investigations.

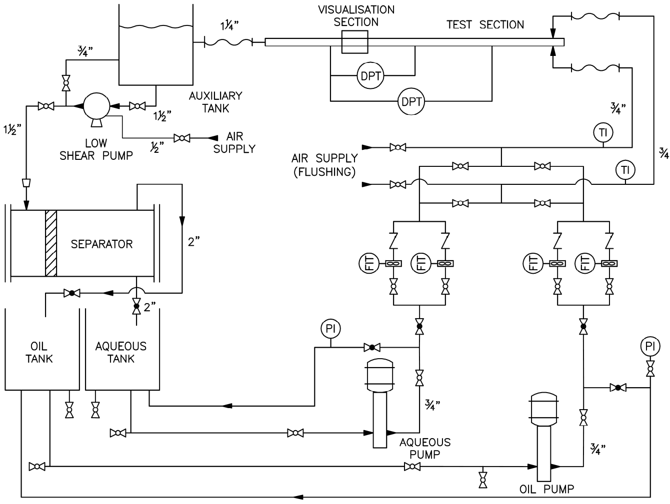

Figure 2 Test flow loop schematic

Table 2 Fluids physical properties

	Oil (Exxsol D140)	Water
Density (kg/m^3)	825	998
Viscosity at 25°C (mPa.s)	5.4	0.9
Interfacial tension (mN/m)	40	

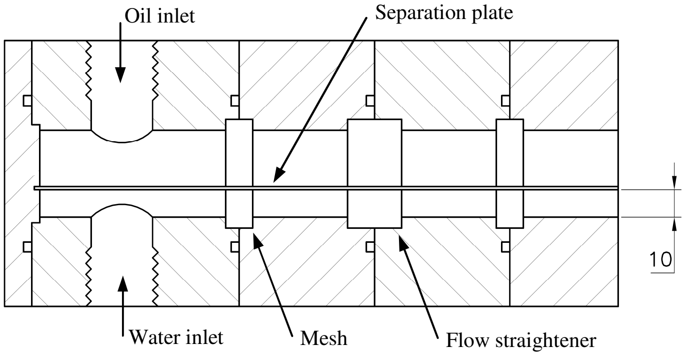

Figure 3 Inlet section schematic for $WC \leq 0.5$

Table 3 Inlet configuration for the current experimental investigations

Water cut	Inlet plate location
$WC \leq 0.5$	10 mm from the bottom of the pipe
$WC > 0.5$	10 mm from the top of the pipe

Experimental investigations have been carried out for various water cuts and mixture velocities. Water cuts were varied from 0.1 to 0.9 and mixture velocities from 0.25 to 1.25 m/s. Flow regime identification was conducted at the visualisation section which was located at 6.7 m form the inlet such that $L/D = 209$. An Olympus iSpeed 2 high-speed camera with a maximum resolution of 800×600 pixels at 1000 fps was utilised to identify the flow regimes. Images were recorder at either 800 or 1000 fps.

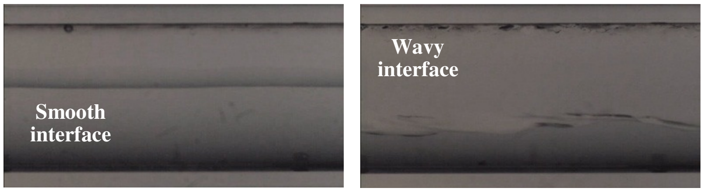

(a) Stratified flow (ST)

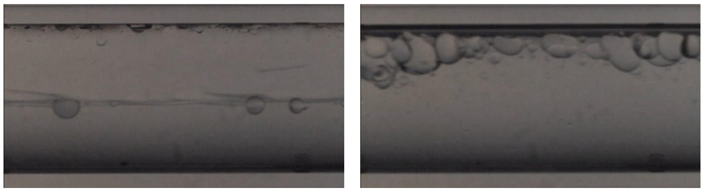

(b) Stratified wavy with droplets at interface (SWD)

(c) Dispersion of oil in water with water layer (DO/W&W)

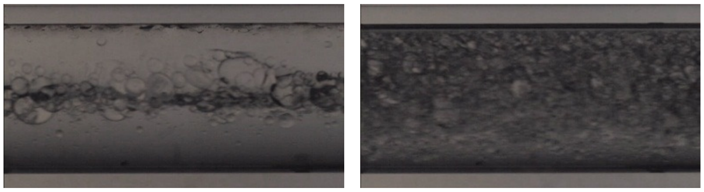

(d) Dual continuous (DC)

(e) Dispersed flow (D)

Figure 4 Instantaneous images of the flow regimes observed in a 32-mm internal diameter horizontal acrylic pipe

RESULTS

Five different flow regimes, as shown Figure 4, were observed in the experimental campaign: (1) stratified flow (smooth or wavy interface), (2) stratified with droplets only at the interface, (3) dispersion of oil in water with a water layer (single continuous), (4) dual continuous (layers of dispersions of oil in water and water in oil), and (5) dispersed flow. From the acquired experimental data, a flow regime map, presented in classical dimensional form in Figure 5, was constructed as a function of the mixture velocity and water cut.

Referring to Figure 5, stratified flows are predominant at low mixture velocities (U_m = 0.25 m/s). As the mixture velocity is increased, instabilities are sufficient enough to break the interface and promote the formation of droplets. These droplets are observed only at the interface for U_m = 0.50-0.75 m/s. At U_m = 0.85 m/s, a transition to dual continuous occurs where droplets of both phases are encountered in the continuous layers of the other phase. Fully dispersed flows are only observed for WC = 0.9 and $U_m > 1.0$ m/s and for WC = 0.5 and $U_m = 1.25$ m/s. Stratified flows are also observed at $WC = 0.2$. This behaviour is attributed to the inlet plate configuration in which the *in situ* water layer height closely matched the height of the inlet plate reducing interface instabilities along the test section.

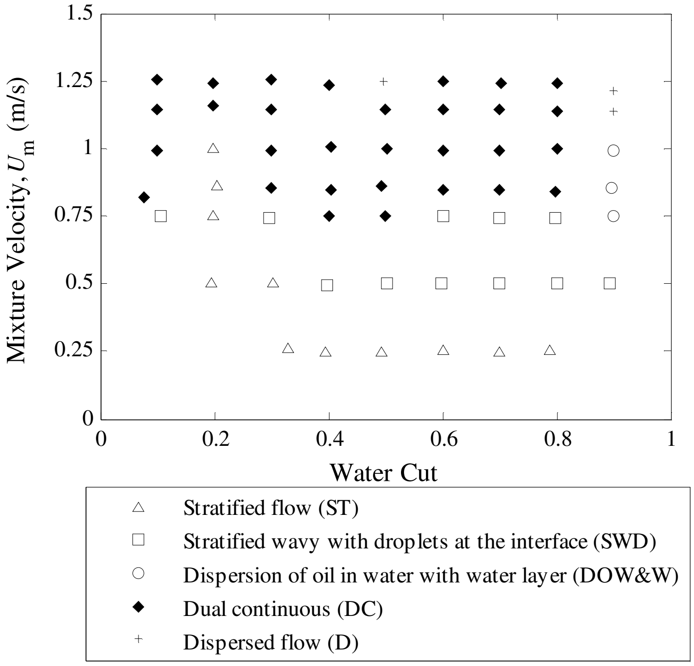

Figure 5 Dimensional flow regime map in a 32-mm internal diameter horizontal acrylic pipe using oil and water

DIMENSIONLESS FLOW REGIME MAPS

Flow regime maps can be drawn by using a dimensional variable basis, such as mixture or superficial velocities, as done in the previous section. The implementation of *dimensionless* flow regime maps can enable a comparison across different studies and the development of a more generalised flow regime transition map applicable to a wide range of flows. The dimensionless groups shown in Table 1 are used here as descriptions of the liquid-liquid flows of interest. From these dimensionless groups, the Reynolds number and the Eotvös number include the governing forces in the flow system: inertial, viscous, gravitational (buoyancy) and capillary forces (interfacial tension). Hence, the effect of fluid properties (i.e. density, viscosity and interfacial tension), flow velocity and pipe diameter are included in these dimensionless parameters.

It was found that a dimensionless flow regime map constructed using the ratio between mixture Reynolds number and Eotvös number as a function of water cut can be employed to characterise the co-current flow of two immiscible liquids. Figures 6 to 8 show the dimensionless flow regime map for the current experimental campaign, as well as data from Lovick and Angeli [11] and Soleimani [12], respectively. In addition, Table 4 summarises of experimental flow conditions that apply to these studies.

Table 4 Summary of experimental condition on horizontal liquid-liquid studies

Authors	D (mm) L/D Test pipe	Inlet type	ρ_w ρ_o (kg/m^3)	μ_w μ_o (mPa.s)	γ (mN/m)
Lovick and Angeli (2004)	38 210 SS	T-Junction (oil inline - water from bottom)	997 828	0.9 6.0	39.6
Soleimani (1999)	24.3 246 SS	T-Junction	997 801	0.9 1.6	17

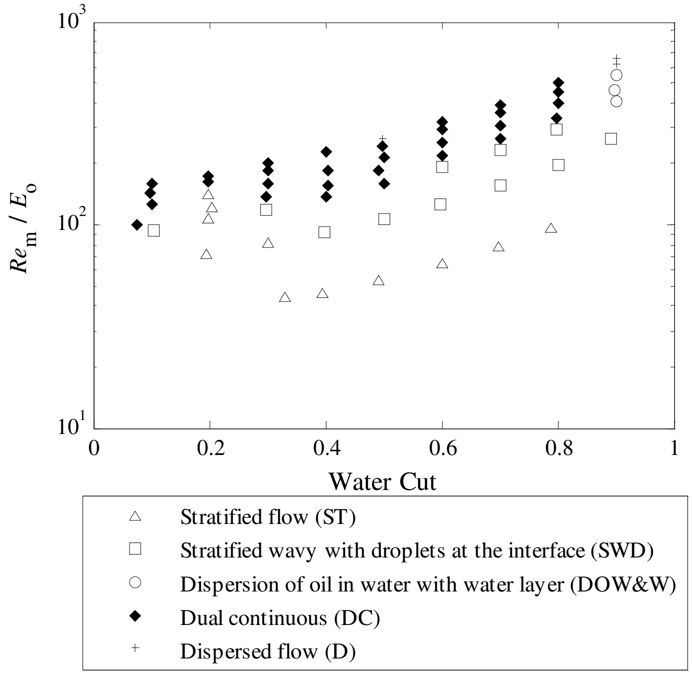

Figure 6 Dimensionless flow regime map in a 32-mm internal diameter horizontal acrylic pipe using oil and water

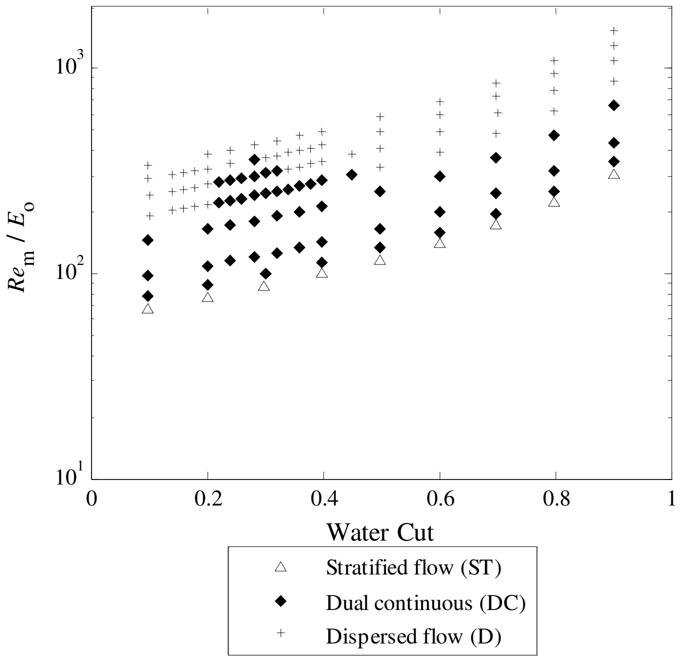

Figure 7 Dimensionless flow regime map in a 38-mm internal diameter horizontal SS pipe (adapted from Lovick and Angeli [11])

The Reynolds number, which is defined as the ratio of inertial forces to viscous forces, offers some insight into the expected velocity field in the flow. Viscous forces are dominant in laminar flows, which can be related to the appearance of stratified liquid-liquid flows. When the inertial forces become dominant, the flow becomes turbulent promoting mixing due to instabilities at the interface. At this point, a transition to non-stratified flows may be expected to occur. The Eotvös number represents the ratio of gravitational (buoyancy) to capillary forces (interfacial tension). Brauner *et al.* [13] found that the interface shape in stratified liquid-liquid flows is a function of the Eotvös number, wettability and the *in situ* phase fractions.

The characterisation of the flow regime transitions in a universal dimensionless flow map must take into account the criteria used to define the flow regimes for each study. Different authors have used different definitions for the liquid-liquid flow regime classification resulting in an overlap when comparing different flow regime maps. For example, Soleimani [12] divided dispersion of oil in water with a water layer (DOW&W) into two sub-categories: single continuous dispersions and dual continuous dispersions (i.e. layers of dispersion of oil in water and dispersion of water on oil). However, dispersions of oil in water with a water layer having one continuous phase are only encountered at high water cuts while the flow regime characterised by layers of dispersion of oil in water and dispersion of water on oil is commonly defined as dual continuous. Lovick and Angeli [11] included the flow regime stratified wavy with droplets at the interface into the dual continuous flow category.

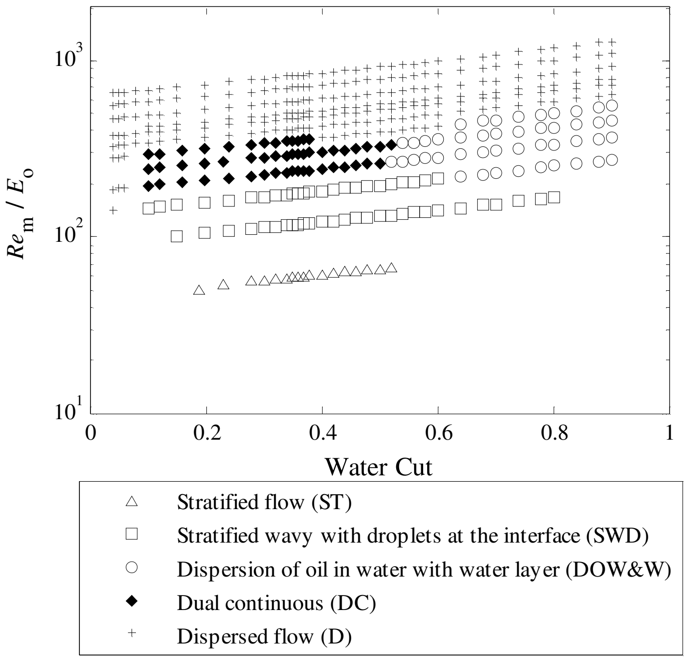

Figure 8 Dimensionless flow regime map in a 24.3-mm internal diameter horizontal SS pipe (adapted from Soleimani [12])

The dimensionless flow regime maps, presented in Figures 6 to 8, show that the transition from stratified flow to non-stratified flow has an upward trend as increasing the water cut. This trend is also observed in Figure 7 and Figure 8 for the transition between dual continuous and dispersed flows. However, only Figure 7 shows a peak in the dual continuous regime at about WC = 0.3. This can represent the inversion point in the flow at which the continuous phase becomes the dispersed phase and vice versa.

Figure 9 shows the final result from the present investigation, which is a dimensionless map of combined flow regime transitions from the analysis of the current experimental data along with the studies form Lovick and Angeli [11] and Soleimani [12]. The flow regime classification was unified to characterise the flow using the classification observed in this study (Figure 4). As increasing the ratio Re_m/Eo for a fixed water cut, transitions from separated flows to dispersed flows are observed. Dispersions of oil in water with a water layer are only encountered for high water cuts and Re_m/Eo between 210 and 800. Stratified flows with droplets at the interface are not observed for low water cuts $WC < 0.1$. At these conditions, a regime transition from stratified flow to dual continuous is observed as increasing Re_m/Eo. This can be attributed to the small water layer height where droplets migrate away from the interface. This phenomenon can also explain the steeper downward trend as decreasing water cut in the transition boundary to dispersed flows for $WC < 0.25$.

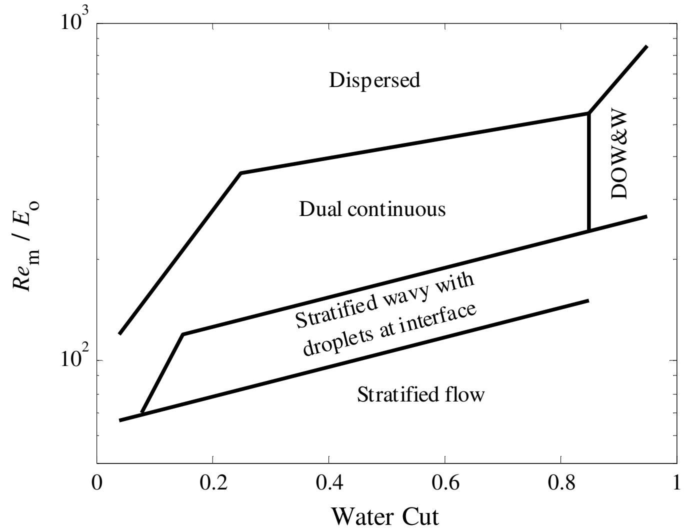

Figure 9 Dimensionless flow regime transitions map

The effect of the *in situ* phase fraction on the flow behaviour has not been included in the above approach as this value is similar to the corresponding water cut (i.e. no-slip condition) for horizontal flows. For inclined flows, the *in situ* phase fraction needs to be included in the flow analysis as the slippage between both phases increases. The Reynolds number expression can be redefined to incorporate the *in situ* fluid velocities.

CONCLUSION

Experimental data have been acquired in a 32-mm internal diameter horizontal acrylic pipe using initially stratified flow of water and Exxsol D140 as the oil phase. Flow regimes were identified using instantaneous images of the flow from a high-speed camera. A dimensional flow regime map was constructed for different flow velocities and phase fractions, which showed five different flow regimes: (1) stratified flow (smooth or wavy interface), (2) stratified with droplets at the interface, (3) dispersion of oil in water with a water layer, (4) dual continuous, and (5) dispersed flow.

A dimensional analysis was carried out to characterise the liquid-liquid flow system under investigation using dimensionless groups from the knowledge of the relevant independent flow-system variables. Based on these dimensionless groups, the flow regime transitions for the analysed experimental data were described by the ratio of the mixture Reynolds number to the Eotvös number, plotted as a function of the water cut. These dimensionless numbers represent the key governing forces in the flow system (i.e. inertial, viscous, gravitational and capillary forces) and include the relevant variables in horizontal liquid-liquid flows (i.e. fluid properties, flow velocities and pipe sizes).

The developed dimensionless flow regime transition map enables the identification of flow regimes for different conditions, namely, flow velocities, fluid properties and pipe sizes. While it is true that the flow map was constructed from the implementation of dimensionless parameters, the flow regime transitions were based on experimental data. Therefore, the applicability of the dimensionless transition map is limited to the data available. Beyond the data generated in the present study, additional data from two references were also used [11,12]. It is noted that the criteria used to classify flow regimes differ for different studies complicating the comparison of liquid-liquid flow regimes maps. Extension to different conditions requires further analysis, while application of the proposed regime map to new (or existing) sets of data can help refine and verify the effectiveness of the map.

ACKNOWELDGEMENTS

This work has been undertaken within the Consortium on Transient and Complex Multiphase Flows and Flow Assurance (TMF). The authors gratefully acknowledge the contributions made to this project by the UK Engineering and Physical Sciences Research Council (EPSRC) and the following: ASCOMP, BP Exploration; Cameron Technology & Development; CD adapco; Chevron; KBC (FEESA); FMC Technologies; INTECSEA; Granherne; Institutt for Energiteknikk (IFE); Kongsberg Oil & Gas Technologies; MSi Kenny; Petrobras; Schlumberger Information Solutions; Shell; SINTEF; Statoil and TOTAL. Thanks are extended to Hannah Moran and Samuel Cockman for their support during the experimental investigation stage.

REFERENCES

[1] Russell, T. W. F., Hodgson, G. W. and Govier, G. W., Horizontal pipeline flow of mixtures of oil and water. *Can. J. Chem. Eng.*, Vol. 37, No. 1, 1959, pp. 9-17

[2] Charles, M. E., Govier, G. W. and Hodgson, G. W., The horizontal pipeline flow of equal density oil-water mixtures. *Can. J. Chem. Eng.*, Vol. 39, No. 1, 1961, pp. 27-36

[3] Oglesby, K.D., An Experimental Study on the Effects of Oil Viscosity Mixture Velocity, and Water Fraction on Horizontal Oil-Water Flow, *M.S. thesis,* The University of Tulsa, 1979

[4] Trallero, J.L., Oil-Water Flow Pattern in Horizontal Pipes. *Ph.D. thesis*, The University of Tulsa, 1995

[5] Baker, O., Design of pipelines for the simultaneous flow of oil and gas. *Oil and Gas Journal*, Vol. 53, 1954, pp.185-195

[6] Beggs, H.D. and Brill, J.P., A study of two-phase flow in inclined pipes. *J. Pet. Tech.,*1973, 607-617

[7] Weisman, J. and Kang, S.Y., Flow pattern transitions in vertical and upwardly inclined lines. *Int. J. Multiphase Flow*, Vol. 7, 1981, pp. 271-291

[8] Brennen, C.E., Fundamentals of multiphase flows. Cambridge University Press, 2009

[9] Awad, M.M., Two-phase flow. In: Kazi, S.N. *An overview of heat transfer phenomena*. Intech, 2012, pp. 251-340

[10] Dukler, A.E., Wicks, M., Cleveland, R.G., Pressure drop and hold-up in two-phase flow. *AIChE J.* Vol. 10, 1964, pp. 38-51

[11] Lovick, J. and Angeli, P., Experimental studies on the dual continuous flow pattern in oil-water flows. *Int. J. Multiphase Flow*, Vol. 30, 2004, pp. 139-157

[12] Soleimani, A., Phase Distribution and Associated Phenomena in Oil-Water Flows in Horizontal Tubes, *Ph.D. thesis*, Imperial College London, 1999

[13] Brauner, N., Moalem Maron, D., and Rovinsky, J., A two-fluid model for stratified flows with curved interfaces. *Int. J. Multiphase Flow*, Vol. 24, 1998, pp. 975-1004

APPLICATION OF THE TURBULENCE-RESOLVING FINITE-SIZE LAGRANGIAN METHOD TO A BUBBLE COLUMN REACTOR

Badreddine H., Niceno B.* and Prasser H.M.
*Author for correspondence
Nuclear Energy and Safety Research Department,
Paul Scherrer Institute,
Villigen PSI, 5232,
Switzerland,
E-mail: bojan.niceno@psi.ch

ABSTRACT

In this work, we present the latest developments in the finite-size Lagrangian (FSL) tracking method we have recently proposed. The FSL method covers the situations in which dispersed-phase interfaces (bubbles or droplets) are larger than individual computational cells used in simulation, and thus not amenable by Lagrangian particle tracking (LPT). But in the same time, these interfaces are not large enough to be accurately simulated with interface tracking (IT) methods for a given mesh. The FSL method thus covers the middle ground between LPT and IT methods. The FSL method also inherits properties of the two; bubbles' shapes and sizes are prescribed with a phase indicator function and the continuous phase is resolved in Eulerian single-fluid framework as it would be in an IT method, and yet, the forces on individual bubbles are corrected from hydrodynamic force correlations used in LPT methods. After the initial phase of the FSL method verification, which was mainly focused on simulations of single moving bubbles and is published elsewhere, we now apply it to simulation of the real case of a square bubble column reactor, and compare liquid and air velocities and liquid velocity fluctuations profiles against experiments. The distinct advantage of the FSL method, over the standard LPT, is the explicit resolution of turbulent structures, including the wakes behind individual bubbles. Bubble plume meandering was captured well in the simulations, as well as time-averaged vertical velocities. In addition, we broaden the class of multiphase situations we can deal with by coupling the FSL with an IT method. This extended methodology is demonstrated with cases of individual bubbles and droplets merging with a free surface.

INTRODUCTION

Dispersed flows are encountered in a broad spectrum of fields, and understanding their dynamics and how they affect the continuous phase is crucial for safe and efficient operation of many technical devices. For example, dispersed bubbly flow is the operational mode of bubble column reactors, which are widely used in chemical, biological, and petrochemical industries [1], as well as in biological wastewater treatment [2].

Lagrangian particle tracking approach was successfully applied to simulate bubble column reactors in two and three dimensions, operating in laminar and turbulent flow regimes [3, 4, 5]. In these models, a volume-averaged mass and momentum equations are solved for the continuum phase. Bubbles are tracked in Lagrangian fashion by solving Newton's second law of motion for each particle, or cluster of particles. Two-way coupling (*i.e.* bubbles' influence on the liquid) is accomplished via the liquid volume fraction and the interface momentum transfer incorporated as a source term in the momentum equations. One drawback of these models is the limitation in the number of particles that can be tracked due to the available computer memory. Another drawback is the requirement that bubbles should be smaller than the grid cell size. This is because the liquid volume fraction for each cell should be strictly positive in order to solve the liquid-momentum equations. Furthermore, the mapping techniques used to transfer quantities, such as velocity and pressure gradient, between the Eulerian and Lagrangian frames require that the bubbles should be smaller than the grid cell size. For these reasons, simulations of bubble column reactors have used coarse meshes, so that the bubbles are smaller than the grid cell sizes. This poses problems for mesh refinement studies, bubbles' coalescence, and for simulating bubbles close to the walls where a fine mesh is required.

A new methodology, which authors refer to as finite size Lagrangian (FSL) particle tracking, and inherits features of LPT and IT methods, was proposed to simulate finite-size bubbles whose diameter is larger than the grid cell but not well resolved for accurate IT [6]. It was tested for a single air bubble rising in stagnant water and in linear shear flow with grid cell size ranges from five to twenty cells per bubble diameter. The results, in terms of bubbles' velocity, internal circulation, and the two-way coupling were in good agreements with results simulated with finely resolved interface tracking approach.

In this work, the FSL method is extended to simulate finite-size bubbles or droplets impacting with a free surface. The simulation of a finite-size water droplet with a water surface is taken as a test case. The droplet was selected in purpose instead of a bubble to show the capability of FSL to simulate finite-size droplets. The finite-size droplet is simulated with FSL approach, and the free surface with an IT method. Once the droplet merges with the free surface, the whole system is solved with the IT. Then, simulations of a square bubble column reactor simulated using FSL are presented. Two different lift coefficients are tested, and results are compared to experimental data.

NOMENCLATURE

d	[m]	Distance
dt	[s]	Time increment
f	[N m^{-3}]	Force per unit volume
g	[ms^{-2}]	Gravitational constant
n	[-]	Normal vector
p	[N m^{-2}]	Pressure
R	[m]	Radius
u	[m/s]	Flow velocity vector
V	[m/s]	Bubble velocity vector
V	[m^3]	Volume
C_D	[-]	Drag coefficient
C_L	[-]	Lift coefficient
C_W	[-]	Wall coefficient
C_{AM}	[-]	Added mass coefficient
x	[m]	Coordinate in the x direction
y	[m]	Coordinate in the y direction
z	[m]	Coordinate in the z direction

Special characters

Δ	[m]	Grid cell size
ε	[m]	Interface thickness
μ	[Pa s]	Viscosity
ρ	[Kg m^{-3}]	Density
ϕ	[-]	Color function

Subscripts

b	Bubble
disp	Dispersed
drop	Droplet
sep	Separated
r	Relative
l	Liquid
g	Gas
W	Wall
AM	Added mass
cor	Correcting
c	Center of the grid cell
n	Time step n

FINITE SIZE LAGRANGIAN PARTICLE TRACKING

In this section, FSL approach is summarized. For a more comprehensive description, reader is referred to [6]. A single-set of governing equations based on Navier-Stokes equations is solved for the whole domain, *i.e.* the single-fluid approach is used. It is formulated in terms of continuity and momentum equations, defined as:

$$\nabla.\mathbf{u} = 0,$$

$$\frac{\partial(\rho\mathbf{u})}{\partial t} + \nabla.(\rho\mathbf{u}\mathbf{u}) = -\nabla p + \nabla.\{\mu(\nabla\mathbf{u} + (\nabla\mathbf{u})^T\} + \rho\mathbf{g} + \mathbf{f}_{cor}. \quad (1)$$

The mixture density and viscosity are defined as:

$$\rho = \phi\rho_l + (1-\phi)\rho_g,$$
$$\mu = \phi\mu_l + (1-\phi)\mu_g, \quad (2)$$

where ϕ is the color function defined as liquid volume fraction. This means it is one in a cell fully in the liquid, zero in a cell fully in the gas. A smoothed sine profile for the interface is used:

$$\phi_b = \frac{1}{2}\left(1 + \frac{d}{\varepsilon} + \frac{1}{\pi}\sin\left(\frac{\pi d}{\varepsilon}\right)\right), \quad (3)$$

where ε is taken to 1.5 Δ, with Δ is the grid cell size, and *d* is the distance from the bubble's interface to the cell's center (x_c, y_c, z_c):

$$d = \sqrt{(x_b - x_c)^2 + (y_b - y_c)^2 + (z_b - z_c)^2} - R_b. \quad (4)$$

It should be noted that equation (3) is applied for interfacial cells with $|d| \leq \varepsilon$, and it is valid for bubbly flows. In case of droplets, the color function $\phi_{\text{drop}} = 1 - \phi_{\text{b}}$ should be used.

Bubbles' (or droplets) shape is imposed rather than calculated from the balance of surface tension with other forces acting on a bubble. A spherical shape is used. Therefore, the surface tension force is not included in the momentum equations. Thanks to this simplification, currents and small time increments required in models with surface tension force are avoided.

The second feature of FSL is the introduction of the correcting force $\mathbf{f}_{\text{cor}}$ that is included in the momentum equations to reduce the error in the relative bubble velocity due to poor resolution of individual bubbles. It should be noted that this force is unnecessary for IT because the forces acting on the interface are resolved on the computational grid. The correcting force takes the following form:

$$\mathbf{f}_{cor} = \langle\rho\rangle\frac{\mathbf{v}^{n+1} - \langle\mathbf{u}\rangle}{dt}\Phi_{disp}, \quad (5)$$

where <ρ> and <**u**> are the volume-averaged density and velocity over the bubble (droplet) volume, respectively. This force is added to the cells that are inside the dispersed phase (bubbles or droplets), and it is taken into account by the dispersed volume fraction ϕ_{disp}. For bubbles, $\phi_{disp}=1 - \phi_b$, and in case of droplets $\phi_{disp} = \phi_{drop}$.

Bubble's velocity is calculated from the hydrodynamic forces acting on it. These forces are theoretical with empirical correlations. The equation that governs the motion of the bubbles is Newton's second law given by:

$$(\rho_b + C_{AM}\rho_l)V_b\frac{d\mathbf{v}}{dt} = (\rho_b - \rho_l)V_b\mathbf{g} + \frac{1}{2}\rho_l C_D \pi R_b^2|\mathbf{u}_r|\mathbf{u}_r + C_L\rho_l V_b\mathbf{u}_r \times rot\,\mathbf{u}_l + C_{AM}\rho_l V_b\frac{D\mathbf{u}_l}{Dt} - C_W\rho_l V_b\left(\mathbf{u}_r - (\mathbf{u}_r\cdot\mathbf{n}_W)\mathbf{n}_W\right)^2\mathbf{n}_W, \quad (6)$$

where the first term on the right hand side of the equation is the buoyancy force, the second the drag, the third the added mass force, and the fourth term is the wall lubrication force. The added mass coefficient C_{AM} is taken to 0.5 and the wall force coefficient C_W proposed by Hosokawa and Tomiyama [7] is used. The drag and lift coefficients will be specified for each simulation shown in the next sections. In order to calculate the hydrodynamic forces, the undisturbed liquid velocity at the bubble's center is required. For LPT models, since the bubble is smaller than the grid cell size, the undisturbed liquid velocity is interpolated to the bubble's location from the grid resolved liquid velocity. An extension of this method was developed in FSL [6], and based on creating a "pseudo cubic box" of dimension $3R_b$ around each bubble (Figure 1). The velocity components at the bubble's center are calculated by linear averaging the velocities at the faces' center of the pseudo-box.

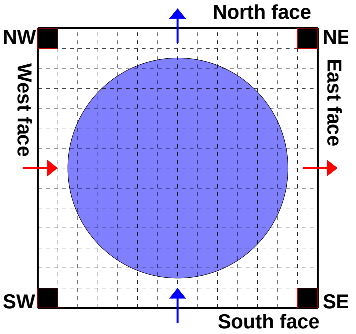

Figure 1 A two-dimensional "pseudo-cell". The red and blue vectors at the middle of the face are used to determine the undisturbed liquid velocity at bubble's centre. They are calculated from the velocities at the corners.

COUPLING FINITE SIZE BUBBLES WITH SURFACE

Finite size Lagrangian method is extended to simulate a dispersed phase (bubble or droplet) merging with a free surface. The dispersed phase is simulated with FSL, while the free surface with an IT approach. In this work, the IT approach based on CIP-CSL2 (constrained interpolation profile; conservative semi Lagrangian scheme; 2nd order) with local sharpening is used [8].

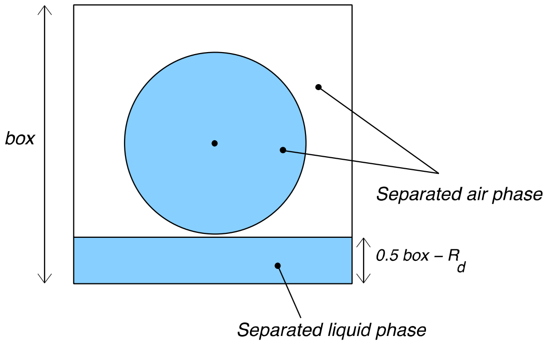

Figure 2 Coupling finite-size droplet with a free surface. The droplet pseudo-box is shown. The numbers in the parentheses (left for ϕ_{drop}, right for ϕ_{sep}) indicate the color function of the dispersed droplet and separated fields, respectively.

In order to clarify the explanation, a droplet merging is considered. The merging criterion used to decide when to merge the dispersed phase with the free surface is based on the volume of separated air phase inside the droplet's pseudo-box (Figure 2). The criterion would be based on the volume of the separated liquid phase. Since the droplet is at the center of the pseudo-box, which is cubic of dimension *box*, the droplet touches the free surface if the volume of the separated liquid phase V_{sep} inside the box becomes larger or equal to the critical volume $V_{critical}$:

$$V_{critical} = box \times \left(\frac{box^2}{2} - R_b \right). \tag{7}$$

Two scalar fields are needed for description of the finite-size droplets with a free surface in the domain: the first one is for the finite-size dispersed droplets, characterized by the color function ϕ_{drop}, and handled by FSL. The second field is for the free surface, characterized by the color function ϕ_{sep}, and tracked with an interface tracking approach. If finite size bubbles exist too in the domain, then additional field (in total three fields) should be added with its own color function ϕ_b.

For any field (separated, droplet, bubbly), the color function is defined in this work as the liquid volume fraction in the cell. First, ϕ_{drop} is initialized to zero (since the continuum is air) in all the cells in the domain regardless of the location of the free surface (Figure 3). Then the color function for the cells that are inside or at droplet's interface is determined as described in the previous section. On the other hand, the color function ϕ_{sep} for the free surface field is initialized with one for the cells that are in the separated liquid and zero in the separated gas regardless of the existence of bubbles and droplets (Figure 4). Then it is updated by solving the advection equation:

$$\frac{\partial \phi_{sep}}{\partial t} + \nabla \cdot (\mathbf{u}\phi_{sep}) = 0. \tag{8}$$

Once the droplet merges with the free surface (Figure 5), it is removed from the dispersed droplet field, and hence will not be tracked using FSL.

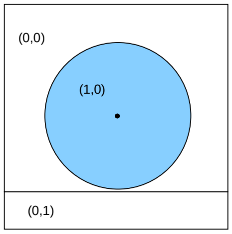

Figure 3 ϕ_{drop} is determined as if the free surface doesn't exist.

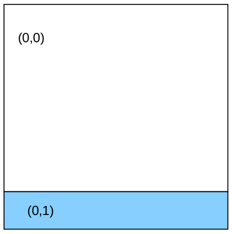

Figure 4 ϕ_{sep} is initialized as if the droplet doesn't exist.

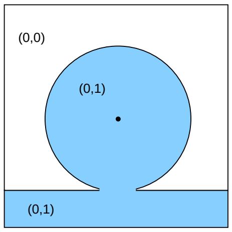

Figure 5 A finite-size droplet merging with a free surface. When merged with the free surface, ϕ_{sep} is set to ϕ_{drop} for cells occupied by the droplet and ϕ_{drop} to zero for the same cells.

The color function ϕ_{sep} for the cells that are inside or at the droplet's interface that is merging with the free surface is modified by taking the value of ϕ_{drop} in these cells. Then ϕ_{drop} for these cells (that were occupied by the merged droplet) is set to zero even though these cells are filled with liquid (since this liquid belongs now to the separated field and not to the dispersed droplet field).

FLOW SOLVER AND ALGORITHM

Every time step in the solver begins first by calling the FSL algorithm. It consists of several steps: first bubble-bubble or bubble-wall collisions are checked. This is done by calculating the minimum time to collision between all the bubbles and between the bubbles and the walls. Then, bubbles are advanced to their new positions using: $\boldsymbol{x}^{n+1} = \boldsymbol{x}^{n} + \mathbf{v}^{n} \Delta t$. This is followed by constructing the pseudo-box for each bubble, and checking the merging criterion with the free surface (if it exists) for each bubble. After this, the hydrodynamic forces acting on each bubble are calculated and the bubbles' new velocities are determined. The color function of the dispersed phase is updated, and the volume-averaged density and velocity for each bubble is calculated. Finally, the correcting force is computed and added as a source term in the momentum conservation equations (Navier-Stokes).

The Navier-Stokes equations are discretized with a semi-implicit projection method in time. Viscous terms are discretized in time with first order backward Euler scheme and the advection terms with the explicit Adams-Bashforth scheme. For the spatial discretization, the orthogonal staggered finite volume method is used; with the second order central difference is used for the diffusive terms and SUPERBEE scheme for the advection terms. First a tentative velocity that doesn't satisfy the continuity equation is obtained using conjugate gradient solver with diagonal preconditioner followed by solving the Poisson equation for the pressure using additive correction multigrid method. The tentative velocity is then projected to divergence free field using the calculated pressure.

Results of a droplet merging with the free surface

This section presents the result of a 2 mm water droplet merging with a free water surface. We refer to this case as to "FSL case" to emphasize that the droplet is simulated with FSL technique. The drag model proposed by Tomiyama *et al.* [9] and the lift model proposed by Tomiyama *et al.* [10] were used here. The computational domain is rectangular channel of dimension $4D_d \times 4D_d \times 8D_d$ in the two lateral (x and y) directions and the vertical z direction, respectively. The physical properties of the air-water system are given in Table 1.

Table 1 Physical properties of air and water used for all the simulations.

	Water	Air
ρ	998.2	1.205
μ	1.00×10^{-3}	1.82×10^{-5}
σ	0.072	

The droplet is resolved with eight cells per diameter, which corresponds to 32 grid cells in the x and y directions, and 64 cells in the z direction. The droplet is initialized at $(0, 0, 0.8L_z)$ with zero velocity while the free surface is initialized at $(0, 0, 0.3L_z)$, where L_z is the channel's length in the vertical direction.

The same problem is also simulated with a well resolved mesh, where both the droplet and the free surface are simulated with CIP-CSL2. We refer to this case as to "CIP case", since the droplet is now simulated with CIP-CSL2. The droplet in this case is resolved with 32 cells per diameter, which corresponds to 128 grid cells in the x and y directions, and 256 cells in the z direction.

The comparison at the time of the droplet impact and afterwards between color functions and between axial vertical velocity from the FSL and CIP cases is shown in Figure 11 and Figure 12, respectively. The FSL case results are in very good agreement with the results obtained with the fully resolved CIP case. This serves as a validation of the correcting force used in FSL for simulating a droplet and of the merging criterion with the free surface. The droplet merging with the free surface is selected in purpose instead of a bubble merging to verify that FSL is also capable of simulating finite-size droplets.

Results of simulations of a square bubble column

Simulations of a square bubble column (Figure 6) that was studied experimentally in [11] are presented in this section. It has a square cross section ($W\times D$) of 0.15×0.15 m^2 and a height (H) of 0.45 m filled with distilled water. Bubbles are created by injecting air with a superficial gas velocity of 4.9 cm/s from the bottom of the column through a perforated plate. The perforated plate contains 7×7 holes with diameter of 1 mm, positioned in the center of the bottom plane of the column with a square pitch of 6.25 mm. The bubbles' diameter is set to 4 mm as observed in the experiment [11]. In the experiment, particle image velocimetry (PIV) was carried with two cameras in order to measure simultaneously the gas and liquid velocities. In order prevent bubble coalescence 4 g of salt per one liter of water was used.

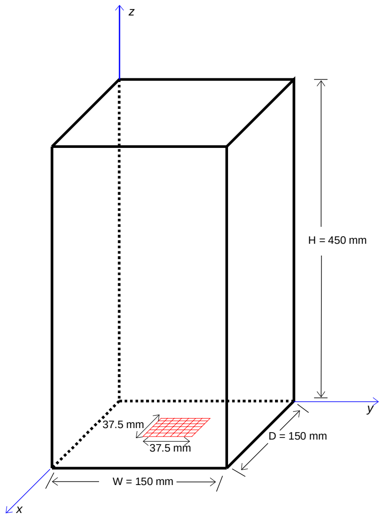

Figure 6 Geometry of the square bubble column used in the simulations.

First, simulations were carried with FSL. The computational grid used in all the simulations is uniform with 152 grid points in the x and y directions, and 456 in the z direction. This corresponds to four grid cells resolution per bubble diameter, and approximately 10.5 million cells in the domain. The bubbles are injected from all the holes every 0.01489 s with a vertical velocity of 0.4 m/s. The bubble period used here can be derived from the total gas volume flow rate Q using the superficial gas velocity V_{sup}: $Q = W \times D \times V_{sup}$. The number of bubbles (N_b) that enter the domain in one second can be then calculated: $N_b = Q / V_{bub} = 3292$ bubbles per second, which corresponds to the injection of 67 bubbles each second from each hole. Wall with no-slip boundary condition was applied to all the boundaries of the domain except the top boundary, which was modeled with a pressure outlet.

All the hydrodynamic forces (drag, lift, added mass, wall lubrication) acting on the bubbles were used. The drag coefficient was set to 0.44 and two lift coefficients were tested: $C_L = 0.15$ and the one from Tomiyama's correlation [10] which corresponds to $C_L = 0.3$ for a 4 mm air bubble in water. The two simulations were stopped after six seconds because the vertical liquid velocity was too high (exceeds 0.6 m/s) as can be seen in Figure 7. This means that the time-averaged vertical liquid velocity will be over-predicted in case the simulations were to be continued. The main reason for getting a high vertical liquid velocity profile comes from the fact that the undisturbed liquid velocity is calculated from the corners of the pseudo-box of each bubble. Since many bubbles are present in the domain, it could occur that some bubbles occupy the corners of the pseudo-box, and contaminate the calculation of the undisturbed liquid velocity. It was observed from the simulations that the bubbles' vertical velocity reached more than 1 m/s. This will also increase the liquid velocity due to the two-way coupling (the correcting force inside the bubbles).

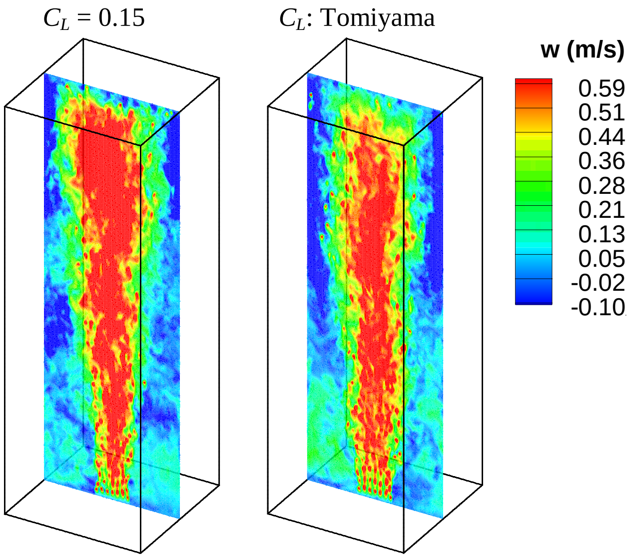

Figure 7 Instantaneous vertical velocity contour at t = 5 s of the square bubble column using FSL for different lift coefficients.

In order to deal with the above problem, a restriction on the bubble's velocity is imposed. First, the bubble's velocity is calculated using the undisturbed liquid velocity from the corners of the pseudo-box. If the calculated bubble velocity is higher than a pre-defined value (in this case it is taken to 0.35 m/s, which is above the terminal rise velocity of a 4 mm air bubble in water), then it is set to this value (0.35 in this case). It should be noted that this restriction is checked for each bubble's velocity component.

The two simulations were repeated with this restriction, and run for 120 seconds. Results were time-averaged from 20 to 120 seconds from data saved each half a second. Each simulation took around one month using 128 Intel Xeon, 2600 MHz, cores. The time-averaged liquid velocity ($\mathbf{u}_l$) and liquid velocity fluctuations (u'_l) for a given grid cell are calculated as follows:

$$\overline{\mathbf{u}}_l = \frac{\sum_{n=20}^{n=120} \mathbf{u}_n \phi_n}{\sum_{n=20}^{n=120} \phi_n},$$

$$\mathbf{u}'_l = \sqrt{\frac{\sum_{n=20}^{n=120} \left(\mathbf{u}_n - \overline{\mathbf{u}}_l\right)^2 \phi_n}{\sum_{n=20}^{n=120} \phi_n}},$$

where ϕ_n is the liquid volume fraction at time step n.

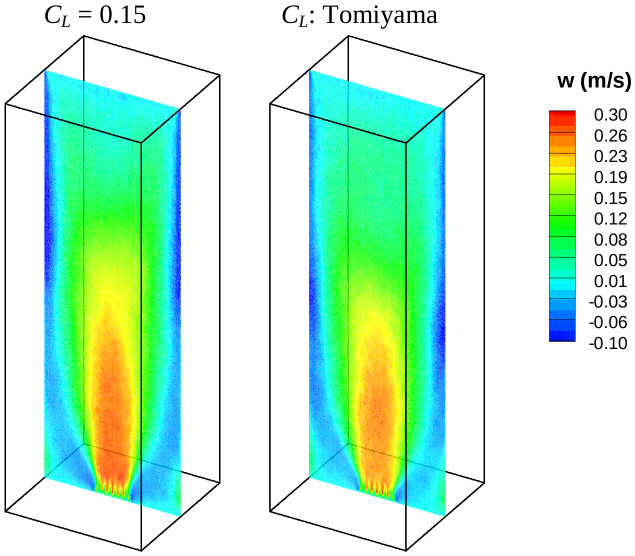

Figure 8 Contour of the time-averaged vertical liquid velocity in a vertical plane of the bubble column using FSL with restricted bubbles' velocities for different lift coefficients.

The contours of the time-averaged vertical liquid velocity for both simulations are shown in Figure 8. The symmetry pattern of the vertical liquid velocity is well predicted, and the backward flow (negative velocity) close to the wall is detected. The reason for the liquid backward flow close to the walls comes from the fact that when the bubbles rise in the bubble column, they drag water behind them to upper regions of the column. Due to continuity, liquid has to flow back down to the lower regions again. It can also be seen that the vertical liquid velocity in the center of the column (the red area) is higher when C_L = 0.15 is used. This is related to the fact that the spreading dynamics of the bubble plume decreases with decreasing the lift coefficient, and hence the vertical velocity in the center increases. This is also noticeable in Figure 9 where the time-averaged vertical liquid velocity from the two simulations is compared to the experimental data. Very good agreement is obtained with C_L = 0.15, whereas the profile of C_L = 0.3 (Tomiyama's correlation) under-predicts the experimental data. Since the bubble plume spreads more with Tomiyama's lift coefficient (C_L = 0.3), more bubbles are expected to be present towards the walls, and by the two-way coupling between the dispersed bubbles and the liquid, the liquid velocity profile away from the center will be higher with C_L = 0.3, which is also detected. The vertical and horizontal liquid fluctuations have the same trend compared to the experiment close to the wall, but they under-predict the experimental data in the center of the bubble column as shown in Figure 10. This could be related to the restriction imposed on the bubbles' velocity. Bubbles' positions at different times of the simulations are shown in Figure 13. The bubble plume meandering is well captured with FSL for both simulations. It can be noticed that the bubble plume is more spread when using Tomiyama lift coefficient, since more lift will produce more spreading. The bubble plume meandering can also be seen in Figure 14, where instantaneous vertical velocity contours at different times are shown. It can be noticed that the bubble plume moves to one side of the domain, with up-flow in the center of the column and down-flow close to the wall opposite to the direction of the bubble plume.

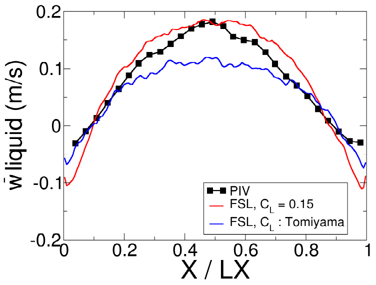

Figure 9 Comparison of simulated (using FSL with restricted bubbles' velocities) and experimental profiles for the time-averaged vertical liquid velocities at a height of z/H = 0.56 and a depth of y/W = 0.5.

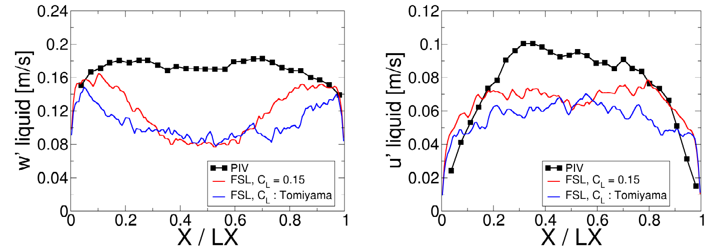

Figure 10 Comparison of simulated (using FSL with restricted bubbles' velocities) and experimental profiles for the time-averaged fluctuating vertical (left) and horizontal (right) liquid velocities at a height of z/H = 0.56 and a depth of y/W = 0.5.

CONCLUSION

The FSL particle tracking approach, previously developed by the present authors, has been extended to simulate a finite-size droplet merging with a free surface. The finite-size droplet was simulated with FSL because it was only resolved with eight cells per diameter. The free surface was tracked with CIP-CSL2 interface tracking approach. A criterion was derived to decide when the droplet should merge with the free surface. This case was compared with a finely resolved case where both the droplet and the free surface were simulated with CIP-CSL2. Results, in terms of color function and axial velocity, at the moment of impact and afterwards were in very good agreement with the finely resolved case.

Simulations of a square bubble column were also carried with FSL. It was observed that bubbles' velocities were exceeding 1 m/s. Due to the two-way coupling, this leads to a high liquid velocity profile. The reason behind these high values is the use of the pseudo-box around each bubble to calculate the undisturbed liquid velocity. Since the flow is dense in the middle of the bubble column, some bubbles were overlaying with the corners of the pseudo-box, thus poisoning the calculation of the undisturbed liquid velocity of the bubble in concern. To overcome this problem, a restriction on the bubbles' velocities was imposed. Simulations were conducted with two different lift coefficients, and the highly dynamic nature of the bubble column was well captured. Very good agreement is obtained with C_L = 0.15 for the time-averaged liquid velocity profile compared to the experimental data. Finally, simulation of bubble column reactor is feasible with FSL, but a better method to calculate the undisturbed liquid velocity without leading to bubbles' velocities restriction is necessary.

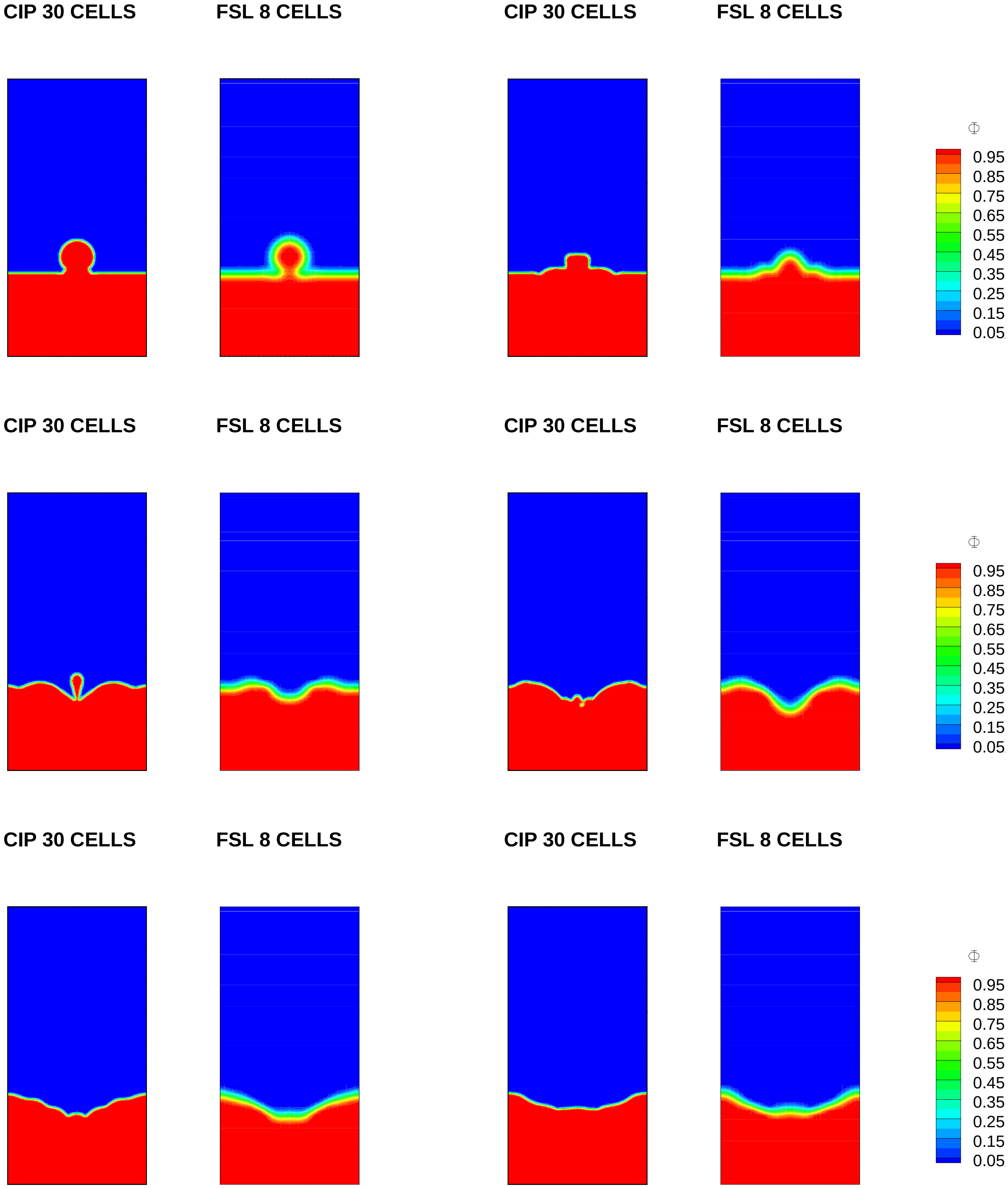

Figure 11 Comparison between color functions from finely resolved CIP-CSL2 (32 cells per bubble diameter) and FSL (eight cells) for a droplet merging with a free surface at the moment of impact and afterwards.

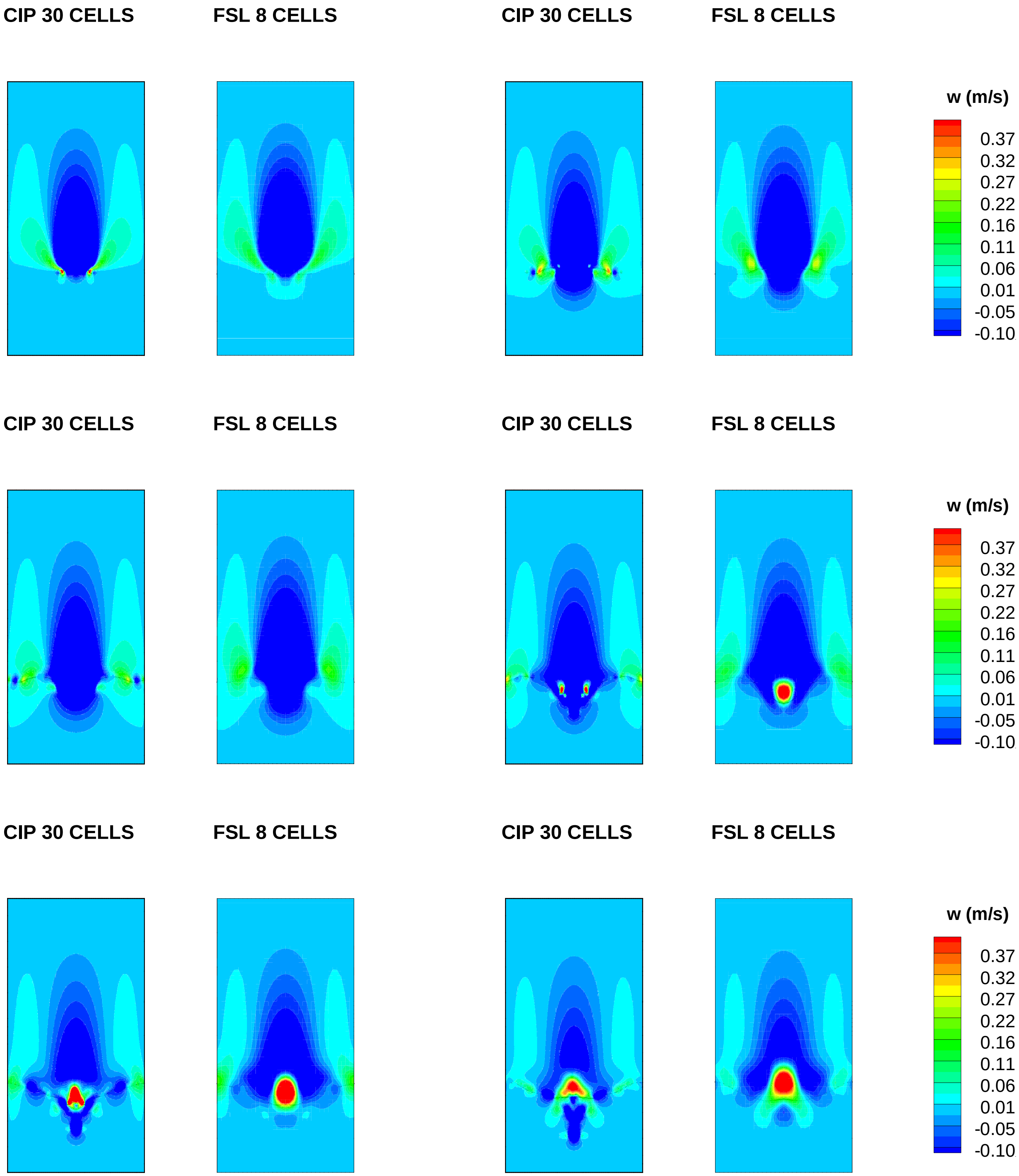

Figure 12 Comparison between axial velocity from finely resolved CIP-CSL2 (32 cells per bubble diameter) and FSL (eight cells) for a droplet merging with a free surface at the moment of impact and afterwards.

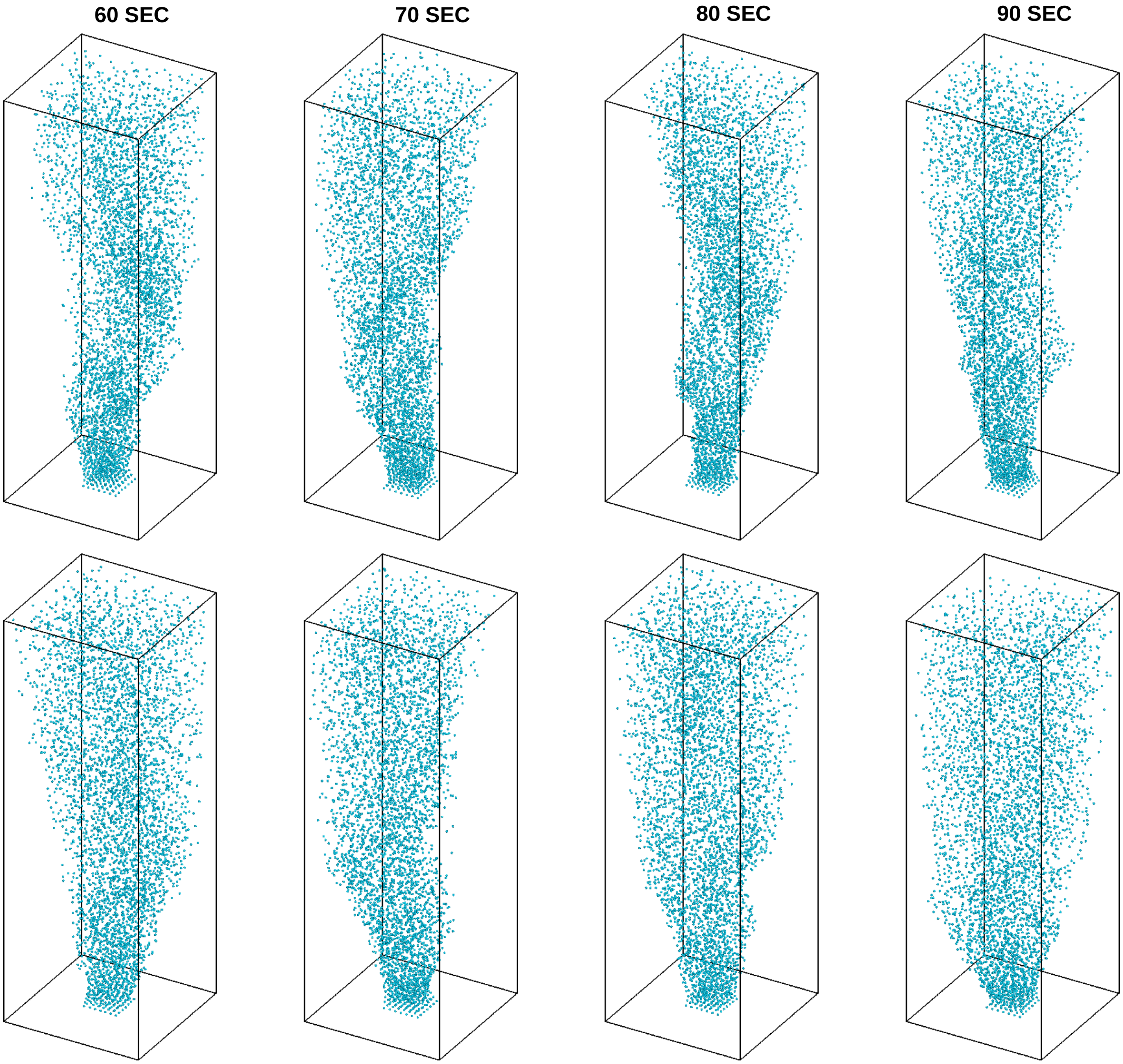

Figure 13 Comparison of snapshots of bubbles' position in the square bubble column at different times simulated with FSL-restricted bubbles' velocities, with C_L = 0.15 (top row) and C_L from Tomiyama's correlation (bottom row).

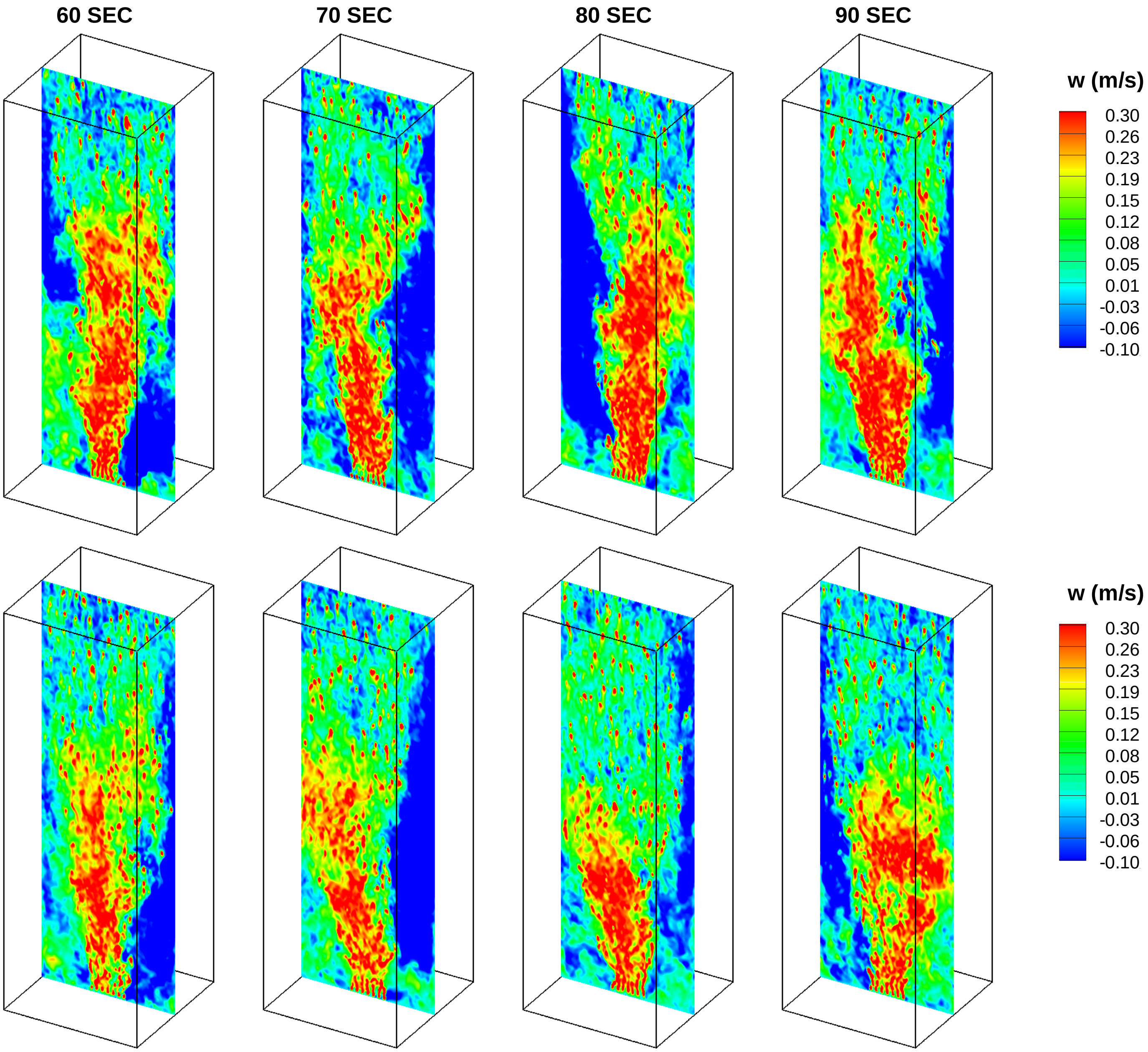

Figure 14 Comparison of instantaneous vertical velocity in the square bubble column at different times simulated with FSL-restricted bubbles' velocities, with C_L = 0.15 (top row) and C_L from Tomiyama's correlation (bottom row).

REFERENCES

[1] Degaleesani S., Dudukovic M., and Pan Y., Experimental study of gas-injected liquid-flow structures in bubble columns, *AIChe Journal,* Vol. 47, 2001, pp. 1913-1931

[2] Prakash A., Margaritis A., and Li H., Hydrodynamics and local heat treansfer measurements in a bubble column with suspension of yeast, *Biochemical Engineering Journal*, Vol. 9, 2001, pp. 155-163

[3] Delnoij E., Kuipers J., and Van Swaaij W., Dynamic simulation of dispersed gas-liquid two-phase flow using a discrete bubble column, *Chemical Engineering Science,* Vol. 52, 1997, pp. 1429-1458

[4] Darmana D., Deen N., and Kuipers J., Detailed modeling of hydrodynamics, mass transfer and chemical reactions in a bubble column using a discrete bubble model, *Chemical Engineering Science,* Vol. 60, 2005, pp. 3383-3404

[5] Buwa B., Deo D., and Ranade V., Eulerian-Lagrangian simulations of unsteady gas-liquid flows in bubble columns, *International Journal of Multiphase Flow,* Vol. 32, 2006, pp. 864-885

[6] Badreddine H., Yohei S., Niceno B., and Prasser H.M., Finite size Lagrangian particle tracking approach to simulate dispersed bubbly flows, *Chemical Engineering Science,* Vol. 122, 2015, pp. 321-335

[7] Hosokawa S., and Tomiyama A., Lateral force acting on a deformed single bubble due to presence of wall, *Trans. Jpn. Soc. Mech. Eng,* Series. B, 2003, pp. 2214-2220

[8] Sato Y., and Niceno, B., A conservative local interface sharpening scheme for the constrained interpolation profile method, *International Journal for Numerical Methods in Fluids,* Vol. 70, 2011, pp. 441-467

[9] Tomiyama A., Zun, I., Higaki, H, Makino, Y., and Sakaguchi, T., A three-dimensional particle tracking method for bubbly flow simulation, *Nuclear Engineering and Design,* Vol. 175, 1997, pp. 77-86

[10] Tomiyama A., Tamai, H., Zun, I., and Hosokawa, S., Transverse migration of single bubble in simple shear flows, *Trans. Chemical Engineering Science*, Vol. 57, 2002, pp. 1849-1858

[11] Deen N., Solberg, T., and Hjertager, B., Large eddy simulation of the gas-liquid flow in a square cross sectioned bubble column, *Chemical Engineering Science,* Vol. 56, 2001, pp. 6341-4349

MEASURED VOID FRACTION AND HEAT TRANSFER COEFFICIENTS DURING CONDENSATION

Olivier, S.P.[1], Meyer, J.P.[1*], De Paepe, M.[2] and De Kerpel, K.[2]
*Author for correspondence
[1]Department of Mechanical and Aeronautical Engineering,
University of Pretoria,
Pretoria, 0002,
South Africa

[2]Department of Flow, Heat and Combustion Mechanics,
Ghent University – UGent,
Sint-Pietersnieuwstraat 41, 9000
Gent.
Oost-Vlaanderen, Belgium

E-mail: josua.meyer@up.ac.za

ABSTRACT

Most work in literature on condensation in tubes has been done for smooth tubes in the horizontal and vertical configurations. Recent experimental works with condensation at different inclination angles showed that the heat transfer characteristics were a function of inclination angle. These works were limited to heat transfer and pressure drop measurements with visual observations. However, no work has been done on measuring the void fractions during condensation at different inclination angles. The purpose of this study was to measure void fractions and heat transfer coefficients during condensation for tube inclinations ranging from vertical downwards (-90°) to vertical upwards (90°) at a saturation temperature of 40°C. Measurements were taken in an experimental set-up in which condensation occurred on the inside of a test section. The test section was a circular tube with an inner diameter of 8.38 mm and a heat transfer length of 1.488 m. The refrigerant used was R134a, and the void fractions were measured using two capacitive void fraction sensors. A mass flux of 100 kg/m^2.s and vapour qualities ranging from 10 – 90% were considered. Heat transfer coefficients were also compared with void fractions. It was found that at low mass fluxes and vapour qualities, void fraction and heat transfer were significantly affected by changes in inclination angle. Generally, void fractions and heat transfer coefficients increased with downward inclination angles with an optimum angle between -10° and -30° (downward flow). At some vapour quality conditions, the void fraction and heat transfer coefficients were observed to be independent of the inclination angle despite changes in the prevailing flow patterns.

INTRODUCTION

Industries where condensation occurs are in the power generation industries where steam is condensed in air and water cooled cooling towers. In the majority of cases condensation occurs in tubes which are configured horizontally. An exception is steam condensation in large air cooled condensers where water is not readily available as a cooling medium. These condensers are constructed in an A-frame structure configured to provide condensing flow at an approximate 60° downward and upward inclination. However, no work has been published in the open literature that justifies this angle. It is therefore not clear if this angle is based on heat transfer and/or structural considerations.

A recent review of the state of the art in condensation flow was conducted and the conclusion was drawn that the majority of work was done for horizontal tubes and a limited amount in vertical tubes [1]. However, very little work was done for condensation in inclined tubes. Past work have highlighted the importance of the identification of the prevailing flow pattern since it is used in the development of equations that estimate the local and average heat transfer and pressure drop coefficients during condensation [2]–[5].

Past work on the subject of condensation in inclined tubes found that downward inclination angles could have significant advantages since gravity assisted in thinning the liquid layer inside the tube and reduce the thermal resistance to heat transfer [6].

The heat transfer and pressure drop during condensation in a tube are directly related to the temporal and spatial distribution of the liquid and vapour phases. These phases are directly related to the void fraction and a considerable number of measurements have been taken to relate the void fraction to heat transfer and pressure drop equations during condensation [7]–[9]. However, no work has been done to determine the void fraction and its influence on heat transfer coefficients during condensation in inclined tubes. In addition, no work has been done on the development of new and/or revision of existing equations, which takes into consideration the changes that occur in void fraction as a function of the inclination angle.

Accurate void fraction measurements are challenging, and in most cases where void fractions were measured it was done using only one sensor for the entire test section [10]–[13].

This is perhaps not an accurate representation of the average void fraction of a test section that changes between the inlet and outlet. As the void fractions and heat transfer correlations are so strongly related there is a need for accurate void fraction measurements, however, instrumentation that can measure void fractions without influencing the flow patterns are not readily available commercially. Such a void fraction sensor has been developed at the Ghent University [14]–[17], but is not yet commercially available on the open market.

The purpose of this study was to measure void fractions with two void fraction sensors developed at Ghent University, capture prevailing flow patterns visually and measure the heat transfer coefficients over a wide range of inclination angles during condensation in a smooth tube. The effect of the void fractions on the flow patterns and heat transfer coefficients was also investigated qualitatively.

NOMENCLATURE

A	[m^2]	Cross-sectional flow area/heat transfer surface area
c_p	[J/kg.K]	Specific heat at constant pressure
d	[m]	Diameter
EB	[ ]	Energy balance
G	[kg/m^2.s]	Mass flux
h	[J/kg]	Specific enthalpy
k	[W/m.K]	Thermal conductivity
L	[m]	Heat transfer length of test section
$\dot{m}$	[kg/s]	Mass flow rate
$\dot{Q}$	[W]	Heat transfer rate
R	[m.K/W]	Thermal resistance
T	[°C]	Temperature
V	[V]	Voltage
x	[ ]	Vapour quality
z	[m]	Axial tube dimension
Special characters		
α	[W/m^2.s]	Heat transfer coefficient
Subscripts		
Cu		Copper
f		Saturated liquid state
g		Saturated vapour state
H_2O		Water side
i		Inner/inlet
j		Counter index
L		Liquid
$Norm$		Normalised
o		Outside/outlet
$PreCond$		Pre-condenser
V		Vapour
R		Refrigerant side
sat		Saturation state
$Test$		Test section
$System$		System conditions
w		Tube wall
Other		
A		Annular flow pattern
I		Intermittent flow pattern
SL		Slug flow pattern
C		Churn flow pattern
C/SA		Churn semi-annular flow pattern
SW		Stratified-wavy flow pattern

EXPERIMENTAL APPARATUS AND TEST CONDITIONS

EXPERIMENTAL SET-UP

The experimental system was inherited from past research work; detailed descriptions and explanations of the experimental system have been provided [6]–[9], [14], [18]–[21]. Therefore, only a brief overview will be provided in this section.

The experimental set-up consisted of a vapour compression refrigeration cycle operated with refrigerant R134a, as well as a water cycle. The refrigeration cycle consisted of two high-pressure lines, i.e. the test line and bypass line, through which the condensing fluid was pumped. Fluid flow was obtained using a hermetically sealed scroll compressor with a nominal cooling capacity of 10 kW. The flow of refrigerant through each respective line was controlled using a set of electronic expansion valves (EEVs).

The test line was served by three respective condensers. A pre-condenser was responsible for controlling the vapour quality at the inlet of the test condenser where temperature, pressure, flow pattern and void fraction measurements were taken. Two void fraction sensors were used, one at the inlet of the test section and the other at the outlet of the test section. The average of the two measurements was taken as the average void faction in the test section.

A post-condenser ensured that the refrigerant reached the EEVs in a liquid state to ensure accurate mass flow measurements. The bypass condenser controlled the mass flow rate, saturation temperature as well as saturation pressure of the refrigerant in the test section. The bypass condenser was also adjusted so only liquid refrigerant reached the EEV. Downstream of the respective EEVs, the test and bypass lines merged into a single lower-pressure line, which led to the suction of the scroll compressor through an evaporator. A suction accumulator ensured that only vapour was available at the compressor suction.

Hot and cold water was supplied by a 50 kW heating and 70 kW cooling dual-function heat pump. Thermostat control was used to maintain the hot water at 25°C - 30°C and the cold water at 15°C - 25°C respectively in two tanks of 5 000 litre capacity each. The hot water was used in the evaporator while the cold water was used in the various condensers mentioned previously.

The test condenser was constructed as a tube-in-tube counterflow heat exchanger with refrigerant flowing in the inner tube and water flowing in the annulus. The inner tube was constructed from an 8.38 mm inner diameter (0.6 ± 0.002 mm wall thickness) smooth, hard-drawn copper tube inside an outer tube from 15.9 mm inner diameter smooth, hard-drawn copper tube. The refrigerant stream flowed through the inner tube and the water stream through the annulus in a counter flow direction. A wire with an outside diameter of 2 mm was wrapped around the outside of the inner tube at a constant pitch to improve water mixing within the annulus and prevent temperature stratification. The heat transfer length of the test section was measured as 1.488 m. The entire test section was insulated with 60 mm thick insulation with a thermal conductivity of 0.041 W/m.K to minimise heat losses to the ambient air. The inclination angle was measured using a digital inclinometer that was attached at the pivot point of the test section.

To develop the flow as fully as possible at the inlet to the test section a calming section with a length of 260 mm (31 tube diameters) was situated upstream of the test section. Space limitations prevented any further increase in length of the test section.

Borosilicate sight glasses were installed at both the inlet and outlet of the test section, which enabled visual observation of the flow patterns. The sight glasses also insulated the test section against axial heat conduction. A monochromatic high-speed camera set at roughly 200 frames per second was used at the outlet sight glass for flow visualization. To improve the image quality, a uniform light emitting diode (LED) backlight was used. The LED backlight was chosen with a low energy output so that it did not thermally affect the passing flow.

Three pressure taps were installed at both the inlet and outlet of the test section respectively. They were affixed to the tube by silver soldering ±20 mm long capillary tubes on each end of the test section. A 1 mm hole was drilled through the capillary tube through the tube wall of the test section. A small diameter was desirable to ensure that the pressure taps did not cause flow obstructions in the test section and that the diameter was less than 10% of the test section's inner diameter [22]. Care was taken to remove all burrs from the inside of the test section which may have an undesirable effect on pressure measurements.

Two of the aforementioned taps were connected to ratiometric pressure transducers, which measured the prevailing absolute pressure at both the inlet and outlet of the test section respectively. The remaining pressure taps were available for differential pressure measurement, which was not considered for the current study. The pressure sensors used to measure the saturation pressure was calibrated and had an uncertainty of 0.1% relative to its full scale of 3 447 Pa.

On the outer periphery of the inner tube, four countersunk indentations were drilled to enable the thermocouples to be affixed by soldering. The indentations were equally spaced around the periphery in such a way that two thermocouples could be located on a plane perpendicular to a stratified liquid interface and two in parallel to form a measuring station. There were seven equidistant measuring stations along the length of the test section. All thermocouples were constructed using T-type thermocouple wire with a 30-gauge thickness (0.1 mm) and were calibrated to within ±0.1°C against a PT100 RTD-device.

Three thermocouples were installed upstream of the inlet sight glass and downstream of the outlet sight glass to measure the prevailing saturation temperature. The saturation temperature was also corroborated by the absolute pressure measurements and the REFPROP [23] database for refrigerant R134a. The differences in the measured saturation temperature and those determined from the database using absolute pressure measurements were less than 0.1°C at high mass fluxes, i.e. 400 kg/m^2.s.

The fluid flow rates of the test section, pre-condenser, test condenser and post-condenser were measured using Coriolis mass flow meters with uncertainties of 0.1%. The mass flow meters were installed upstream of each respective condenser. The Coriolis mass flow meter which measured the refrigerant mass flow rate through the test section was situated downstream of the post-condenser and upstream of the EEVs.

The capacitive void fraction sensors used in the current study were developed by Ghent University [14]–[17] and a calibration procedure was developed for adiabatic horizontal flow [13], [24]. For the current study the sensor responses were calibrated to track the predictions of the Rouhani and Axelsson [25] correlation for the case of horizontal adiabatic flow at a saturation temperature of 40°C; good correlation between horizontal adiabatic flow and the Rouhani and Axelsson [25] predictions has been observed in previous work [13].

DATA ACQUISITION AND EXPERIMENTAL PROCEDURE

A computerised data acquisition (DAQ) system was used to gather the data from the respective measuring instruments. The DAQ system consisted of a personal computer using LabVIEW software with which the measurements could be logged and the experimental system could be controlled.

After start-up, adjustments were made incrementally to the experimental system until the desired flow conditions were obtained. The system was allowed to stabilise until all parameters (mass flow rates, temperatures, void fraction measurements and pressures) were visually observed to remain constant and steady-state conditions were achieved. The difference between the heat transfer rate on both the water side and refrigerant side was also monitored as the "energy balance error". Once the energy balance was less than 5% (the average of all measurements was less than 3%), and steady state conditions were achieved measurements were made. The heat transfer rate of the water was assumed to be the more accurate and was controlled by the water mass flow rate and inlet temperature to always be 200 W. This ensured that the heat flux of all the condensation experiments was 10.2 kW/m^2. At the lowest mass flux (100 kg/m^2.s), the energy balances could not always be maintained below 5% and values of up to 6% as an exception were reached.

Data capturing of the heat transfer coefficients and the void fraction results was done individually. The capturing of the heat transfer coefficients preceded the capturing of the void fraction results for each data point. The heat transfer coefficients were captured at a frequency of 1 Hz over a 120-second time span for each data point, after which the void fraction results were immediately acquired at a frequency of 1 000 Hz for a time span of 120 seconds. The sampling frequency was sufficient as most two-phase flow phenomena occur at a frequency of 100 Hz [14]. The Nyquist criterion for sampling was thus satisfied and aliasing of the observed void fraction signals was therefore not a challenge.

DATA REDUCTION

The void fraction results were obtained in a similar fashion to that of past work [13]. The normalised voltage outputs of the capacitive sensors were calculated as follows:

$$V_{Norm} = \frac{V_{Measured} - V_V}{V_L - V_V} \tag{1}$$

The response of each void fraction sensor to an induced liquid-only condition (V_L) were measured at a temperature of 40°C since this differed from the original calibration temperature [13]. The dielectric constant of refrigerant vapour was shown to be temperature independent [26] and thus the vapour-only response (V_V) of the sensors was obtained at ambient temperature only. Using the measured responses for the liquid-only and vapour-only cases, the denominator in equation (1) for the entire data set was determined. This value was assumed to remain constant for the duration of the current study. The numerator in equation (1) was determined using the raw sensor voltage outputs $(V_{measured})$ as well as an ambient vapour-only measurement (V_V), which was taken daily during the data capturing process before any measurements were taken to account for any drift in the void fraction sensors.

A time-average void fraction for each sensor was calculated using a trapezoidal integration routine on the void fraction results for each data point. The average void fraction results were taken as the arithmetic mean between the trapezoidal integrated inlet and outlet void fraction values.

To determine the vapour quality of the fluid at the inlet to the test section, the specific enthalpy at the outlet of the pre-condenser was calculated from the measured heat transfer rate and refrigerant mass flow rates:

$$h_{R,PreCond,o} = h_{R,Test,i} = h_{R,PreCond,i} - \left|\frac{\dot{Q}_{H_2O,PreCond}}{\dot{m}_R}\right| \tag{2}$$

The parameter $h_{R,PreCond}$ was the specific enthalpy of the refrigerant at the inlet and outlet of the pre-condenser (subscripts denote inlet or outlet position), determined from the REFPROP database [23] for the refrigerant R134a. Heat losses between the pre-condenser and test section were neglected; thus the specific enthalpy was assumed to stay constant from the pre-condenser outlet to the test section inlet. The heat transfer through the pre-condenser used in equation (2) was calculated using the measured water mass flow rate, specific heat capacity, and measured water inlet- and outlet temperatures:

$$\dot{Q}_{H_2O,PreCond} = \dot{m}_{H_2O,PreCond}\, c_p \left(T_{PreCond,i} - T_{PreCond,o}\right) \tag{3}$$

The temperature and pressure measurements at the inlet to the test section were used along with a refrigerant property database [23] to determine the saturated liquid and vapour specific enthalpies. The inlet vapour quality was determined as follows:

$$x_{Test,i} = \frac{h_{R,Test,i}}{h_{R,g} - h_{R,f}} \tag{4}$$

The outlet vapour quality was calculated using the inlet specific enthalpy and the heat transfer from the test section as follows:

$$h_{R,Test,o} = h_{R,Test,i} - \left|\frac{\dot{Q}_{H_2O,Test}}{\dot{m}_R}\right| \tag{5}$$

The heat transfer rate through the test condenser was obtained by substituting the parameters in equation (3) for those of the test condenser. The outlet vapour quality was then calculated in a similar fashion to equation (4) by substituting the outlet specific enthalpy calculated from equation (5). The average vapour quality was taken as the arithmetic mean between the calculated inlet and outlet values.

The average heat transfer coefficient in the test section was determined from the wall-, bulk water- and saturation temperature measurements. The water heat transfer rate $(\dot{Q}_{H_2O,Test})$ measurement was used and not the refrigerant heat transfer rate measurement as the water side was considered to be the more accurate of the two heat transfer rate measurements.

Assuming a constant heat transfer coefficient across the length of the test section, the average heat transfer coefficient of the test section was determined as follows:

$$\alpha_{Test} = \left|\frac{\dot{Q}_{H_2O,Test}}{A\left(\overline{T_{w,i}} - T_{sat}\right)}\right| \tag{6}$$

In equation (6) A is the inner surface area of the test section for the heat transfer length and T_{sat} is the saturation temperature calculated as the arithmetic mean between the thermocouple measurements at the inlet and outlet of the test section. An uncertainty analysis [27] showed that the maximum uncertainty of the average heat transfer coefficient was less than 5% with the greatest deviations observed at low vapour quality conditions.

$\overline{T_{w,i}}$ is the mean inner-wall temperature of the test section and is related to the mean outer-wall temperature $\overline{T_{w,o}}$ by the thermal resistance of the tube wall R_w as:

$$\overline{T_{w,i}} = \overline{T_{w,o}} + \left|\dot{Q}_{H_2O,Test} R_w\right| \tag{7}$$

where the thermal resistance of the tube wall was calculated as:

$$R_w = \frac{\ln\left(\frac{d_o}{d_i}\right)}{2\pi k_{Cu} L} \tag{8}$$

The thermal resistance of the tube wall was found to be negligible and therefore it was assumed that the average wall temperature on the outside of the test section was equal to the average wall temperature on the inside of the test section. The mean outer-wall temperature $\left(\overline{T_{w,o}}\right)$ was calculated by averaging the measurements from each of the seven measurement stations along the test section using a trapezoidal integration routine as follows:

$$\overline{T_{w,o}} = \frac{1}{L}\sum_{j=1}^{6}\left[\left(\frac{T_{w,o}^{j} + T_{w,o}^{j+1}}{2}\right)\left(z_{j+1} - z_j\right)\right] \tag{9}$$

In equation (9) z_j is the jth temperature measurement station on the test section.

The energy balance (in percentage) was determined by comparing the heat transferred to the water stream in the annulus of the test section to the heat transfer rate rejected by the condensing refrigerant in the inner tube as:

$$EB_{system} = \left|\frac{\dot{Q}_R - \dot{Q}_{H_2O}}{\left(\dot{Q}_R + \dot{Q}_{H_2O}\right)/2}\right| \times 100 \tag{10}$$

The mass flux was determined from the measured mass flow rate and tube inner cross sectional flow area as:

$$G = \frac{\dot{m}_R}{A} \tag{11}$$

The saturation conditions were controlled with standard deviations of 0.31°C and 9.67 kPa for saturation temperature and saturation pressure respectively. The energy balance was controlled within a 1% standard deviation with an average value of 2.65% for all experimental conditions. The largest deviation (6% heat loss to ambient atmosphere) was observed at the lowest mass flux and vapour quality combinations.

As the current study was a follow-up to work carried out in the past the data population was similar [6], [20]. A lower mass flux case (G = 100 kg/m^2.s) was included because the effect of inclination angle on two-phase flow was expected to be more profound at lower mass fluxes. The experimental data set consisted of 360 data points in total and the data points are shown in Figure 1. The data points are given as function of mass flux, vapour quality and expected flow regime as for a horizontal tube on a modified Wojtan *et al.* [28] flow pattern map with the Kattan *et al.* [29] and Barbieri *et al.* [30] intermittent-annular transition lines. For each data point in Figure 1, measurements were taken at different inclination angles ranging from vertical upward flow to vertical downward flow along with several intermediate inclination angles.

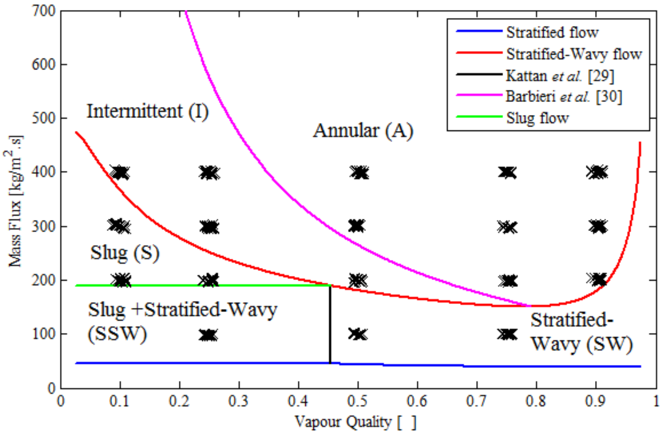

Figure 1 The 360 data points of this study plotted on the modified Wojtan *et al.* [28] flow pattern map

For the lowest mass flux (100 kg/m^2.s), the average vapour quality cases of 10% and 90% were omitted from the data set because the inlet fluid state would be superheated or the outlet fluid state would be sub-cooled to obtain the required average vapour quality. The heat transfer results for the 90% vapour quality case at 300 kg/m^2.s were also omitted as it was found to be unstable and not very repeatable (it may have been because the flow regime condition was close to the point where the flow regime changed from annular flow to stratified wavy flow) as shown in Figure 1.

Observations of the flow patterns were made using high-speed video footage. When the observed flow patterns were adjudged to be a combination of two distinct flow types, a system of naming the flow pattern (as abbreviated in Figure 1 and also defined in the nomenclature list) using a backstroke was adopted. The first abbreviation (before the backstroke) was considered the dominant flow pattern with the second abbreviation a significantly contributing secondary flow pattern effect.

DATA VALIDATION

The void fraction and heat transfer coefficients were validated by taking measurements for the case of horizontal flow with 200 W of condensation heat transfer and comparing the results with literature. Figure 2 presents the measured void fractions for horizontal flow plotted against vapour quality at mass fluxes of 100, 200, 300 and 400 kg-m^2.s. Additionally, the predictions of the Rouhani and Axelsson [25] correlation as well as the prevailing observed flow patterns are also presented. The flow patterns are compared with the flow pattern map of Figure 1.

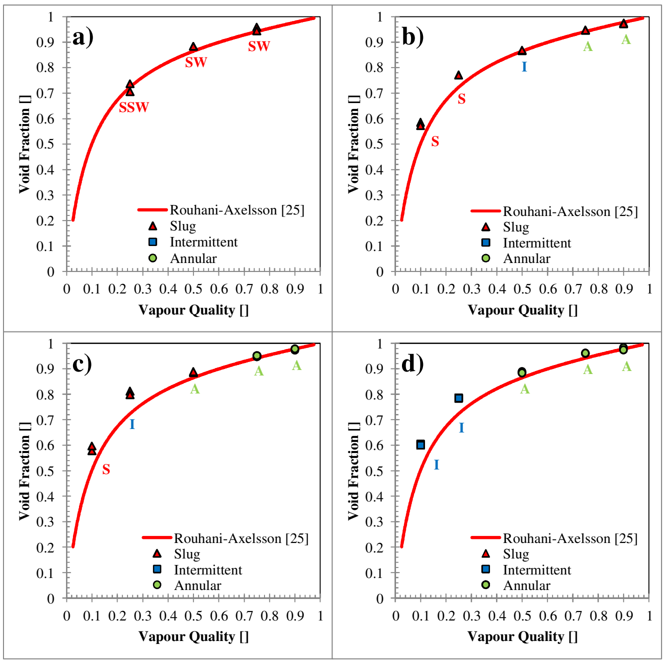

Figure 2 Experimental void fraction measurements as a function of average vapour quality compared with the predictions of the Rouhani and Axelsson [25] void fraction correlation for the case of a horizontal tube for mass fluxes of a) 100 kg/m^2.s, b) 200 kg/m^2.s, c) 300 kg/m^2.s and d) 400 kg/m^2.s. The prevailing flow pattern as observed is indicated by the symbols in the legend. At each data point, the flow pattern predicted by the modified Wojtan *et al.* [28] flow pattern map is indicated using the following abbreviations: Slug (S), stratified-wavy (SW), slug and stratified-Wavy (SSW), intermittent (I) and annular (A). The colour-coding of the abbreviations also correlates with the flow classification of De Kerpel *et al.* [13] in the legend.

In general the horizontal void fraction results correlated well with predictions; all void fraction measurements were predicted within ±5%. Five observed flow patterns out of a total of 18 data points did not match the predictions of the modified Wojtan *et al.* [28] flow pattern map. The aforementioned exceptions could be isolated to the predictions of intermittent flow, which were difficult to classify using subjective visual means.

The measured heat transfer coefficients were also compared with predictions. The comparisons were made using the Thome *et al.* [31] heat transfer correlation using their prescribed logarithmic mean void fraction model as well as the experimentally measured void fractions of this study. Comparisons were also made with the Thome *et al.* [31] correlation making use of the Woldesemayat and Ghajar [32] void fraction predictions and the Cavallini *et al.* [33] heat transfer correlation.

For horizontal flows, 67% of the heat transfer coefficients were predicted within a ±10% error by the Thome *et al.* [31] correlation. At low-heat transfer conditions, i.e. low mass flux and vapour quality, the Thome *et al.* [31] correlation over-predicted the experimental results by about 20–30%. The heat transfer predictions exhibited scatter; this could be the result of the Thome *et al.* [31] correlation's dependence on the void fraction, which varied with the flow configuration.

EFFECT OF INCLINATION ANGLE, VAPOUR QUALITY AND MASS FLUX ON VOID FRACTION AND HEAT TRANSFER

In this study only the mass flux of 100 kg/m^2.s is discussed. The other mass fluxes are discussed in detail in Olivier *et al.* [34]. The measured void fractions for the 100 kg/m^2.s case varied significantly from horizontal flow (0° inclination angle) at 25% vapour quality, even for small adjustments in the inclination angle (Figure 3). The effect of inclination angle on the measured void fractions decreased with increasing vapour quality with the measured void fractions being almost independent of inclination angle for the 75% vapour quality case. The measured void fractions were observed to increase with increasing downward inclination (negative inclination angles) up to a maximum at vertical downward flow. The increase in the measured void fraction could be explained by observing the prevalence of stratified-type flow with the characteristic thin liquid layer as a result of gravity-dominated flow.

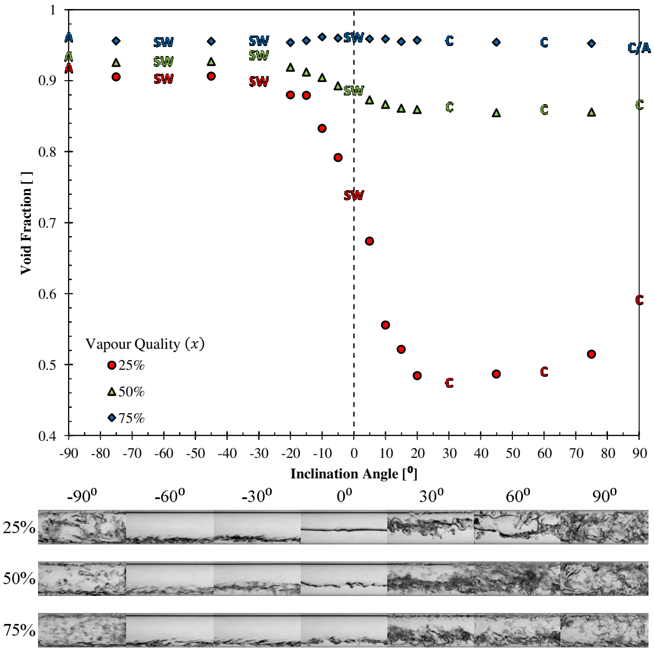

Figure 3 Void fractions as function of test section inclination angle for a mass flux of G = 100 kg/m^2.s and average vapour qualities of 25%, 50% and 75%. The flow pattern abbreviations are A=annular; SW=stratified-wavy; C=churn.

The measured void fractions decreased by 35% compared with horizontal flow for increased upward inclinations (positive inclination angles) up to an inclination of

30° for 25% vapour quality. A similar trend was observed for 50% vapour quality albeit with less profound difference from horizontal flow. The decrease in measured void fractions could be explained by observing the prevailing flow patterns i.e. churn-type flows with liquid recirculation. The greatest degree of recirculating flow corresponded to the minimum measured void fraction. Even though the liquid-vapour distribution was observed to change for the 75% vapour quality case, the measurements indicated that the void fraction remained relatively constant for all inclination angles.

The heat transfer coefficients (Figure 4) were observed to increase significantly with increasing downward inclination up to a maximum in the region of -20° to -15°; a 38% increase relative to horizontal flow was observed for the 25% vapour quality case. The maximum heat transfer coefficients were observed at downward inclination angles where void fractions increased significantly. At these inclination angles, therefore, the thermal resistance was a minimum, i.e. the liquid film thickness was at a minimum as a result of the liquid layer that not only flowed from the top of the tube radially downward, but also forward in the direction of the fluid flow. Further increases in the downward inclination of the flow decreased the measured heat transfer coefficients. Minimum heat transfer was observed at vertical downward flows e.g. a 50% reduction compared with the case of horizontal flow for 75% vapour quality. For vertical downward flows, the thermal resistance was increased exclusively by changes in flow pattern for 50% and 75% vapour quality since the measured void fractions remained relatively constant.

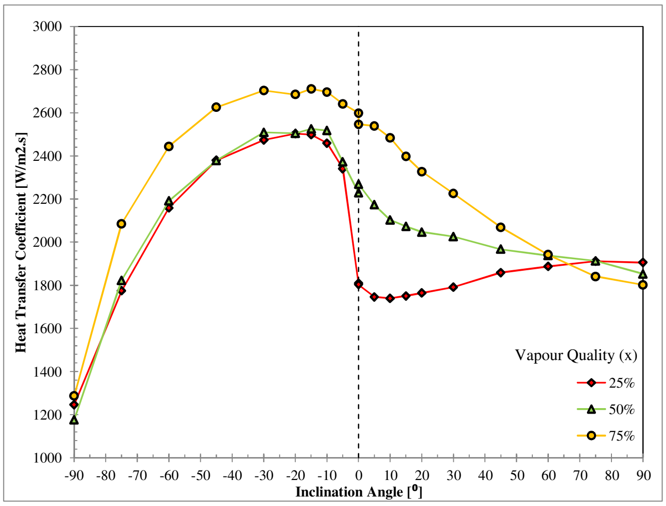

Figure 4 Heat transfer coefficients as a function of inclination angle for a mass flux of G = 100 kg/m^2.s and average vapour qualities of x = 25%, x = 50% and x = 75%.

The heat transfer coefficients were observed to decrease with increased upward inclination angle with the most pronounced inclination effect occurring for 75% vapour quality; a 30% reduction compared with the horizontal case was observed at vertical upward inclination. The reduction in heat transfer was the result of an increase in thermal resistance resulting from a more substantial recirculating liquid layer being present. Increases in upward inclination angle past the minimum increased the measured heat transfer coefficients for the 25% vapour quality case. The increase in heat transfer corroborated with an increase in the measured void fractions for the same inclination angles.

CONCLUSION

The purpose of this study was to measure void fractions of refrigerant R134a condensing in a smooth circular tube with an inner diameter of 8.38 mm and a heat transfer length of 1.488 m. Flow regimes were captured, heat transfer measurements were conducted and void fractions were measured with capacitive void fraction sensors at the inlet and outlet of the test section. The average of the two void fractions was used as the average void fraction of the test section. Measurements were conducted for a full spectrum of inclination angles ranging from vertical downward (-90°) to vertical upward (90°) flow. The void fraction measurements were compared to heat transfer coefficients for a mass flux of 100 kg/m^2.s at vapour qualities ranging from 10–90% with 200 W of condensation heat transfer.

A general independence towards the effect of inclination angle on measured void fractions and heat transfer coefficients was observed with increasing mass flux and vapour quality. The greatest effect of inclination angle on void fractions and heat transfer coefficients were observed for combinations of low mass flux and vapour quality.

Results at downward flow inclinations were affected more profoundly than for upward inclinations. An optimisation opportunity for heat transfer in low vapour quality flows was also identified. The void fraction and flow pattern map predictions were found to be inadequate for inclined flow conditions and scope exists to incorporate gravity-effects in the aforementioned prediction tools.

REFERENCES

[1] S. Lips and J. P. Meyer, “Two-Phase Flow in Inclined Tubes with Specific Reference to Condensation: A Review,” *Int. J. Multiph. Flow*, vol. 37, no. 8, pp. 845–859, Oct. 2011.

[2] S. Nebuloni and J. R. Thome, “Numerical Modeling of the Effects of Oil on Annular Laminar Film Condensation in Minichannels,” *Int. J. Refrig.*, vol. 36, no. 5, pp. 1545–1556, Aug. 2013.

[3] J. R. Thome, A. Bar-Cohen, R. Revellin, and I. Zun, “Unified Mechanistic Multiscale Mapping of Two-Phase Flow Patterns in Microchannels,” *Exp. Therm. Fluid Sci.*, vol. 44, pp. 1–22, Jan. 2013.

[4] E. Da Riva, D. Del Col, S. V. Garimella, and A. Cavallini, “The Importance of Turbulence During Condensation in a Horizontal Circular Minichannel,” *Int. J. Heat Mass Transf.*, vol. 55, no. 13–14, pp. 3470–3481, Jun. 2012.

[5] L. Doretti, C. Zilio, S. Mancin, and A. Cavallini, “Condensation flow patterns inside plain and microfin

tubes: A review," *Int. J. Refrig.*, vol. 36, no. 2, pp. 567–587, Mar. 2013.

[6] S. Lips and J. P. Meyer, "Experimental Study of Convective Condensation in an Inclined Smooth Tube. Part I: Inclination Effect on Flow Pattern and Heat Transfer Coefficient," *Int. J. Heat Mass Transf.*, vol. 55, no. 1–3, pp. 395–404, Jan. 2012.

[7] J. P. Meyer, J. Dirker, and A. O. Adelaja, "Condensation Heat Transfer in Smooth Inclined Tubes for R134a at Different Saturation Temperatures," *Int. J. Heat Mass Transf.*, vol. 70, pp. 515–525, Mar. 2014.

[8] A. O. Adelaja, J. Dirker, and J. P. Meyer, "Convective condensation heat transfer of R134a in tubes at different inclination angles," *Int. J. Green Energy*, 2014.

[9] A. O. Adelaja, J. Dirker, and J. P. Meyer, "Experimental studies of condensation heat transfer in an inclined microfin tube," in *Proceedings of the 15th International Heat Transfer Conference, Kyoto, paper IHTC -9361*, 2014.

[10] M. Demori, V. Ferrari, D. Strazza, and P. Poesio, "A Capacitive Sensor System for the Analysis of Two-Phase Flows of Oil and Conductive Water," *Sensors Actuators A Phys.*, vol. 163, no. 1, pp. 172–179, Sep. 2010.

[11] M. J. Da Silva, S. Thiele, L. Abdulkareem, B. J. Azzopardi, and U. Hampel, "High-Resolution Gas–Oil Two-Phase Flow Visualization with a Capacitance Wire-Mesh Sensor," *Flow Meas. Instrum.*, vol. 21, no. 3, pp. 191–197, Sep. 2010.

[12] W. H. Ahmed, "Experimental investigation of air–oil slug flow using capacitance probes, hot-film anemometer, and image processing," *Int. J. Multiph. Flow*, vol. 37, no. 8, pp. 876–887, Oct. 2011.

[13] K. De Kerpel, B. Ameel, C. T'Joen, H. Canière, and M. De Paepe, "Flow Regime Based Calibration of a Capacitive Void Fraction Sensor for Small Diameter Tubes," *Int. J. Refrig.*, vol. 36, no. 2, pp. 390–401, Mar. 2013.

[14] H. Canière, C. T'Joen, A. Willockx, M. De Paepe, M. Christians, E. Van Rooyen, L. Liebenberg, and J. P. Meyer, "Horizontal Two-Phase Flow Characterization for Small Diameter Tubes with a Capacitance Sensor," *Meas. Sci. Technol.*, vol. 18, no. 9, pp. 2898–2906, Sep. 2007.

[15] H. Canière, C. T'Joen, A. Willockx, and M. De Paepe, "Capacitance Signal Analysis of Horizontal Two-Phase Flow in a Small Diameter Tube," *Exp. Therm. Fluid Sci.*, vol. 32, no. 3, pp. 892–904, 2008.

[16] H. Canière, B. Bauwens, C. T'Joen, and M. De Paepe, "Probabilistic Mapping of Adiabatic Horizontal Two-Phase Flow by Capacitance Signal Feature Clustering," *Int. J. Multiph. Flow*, vol. 35, no. 7, pp. 650–660, Jul. 2009.

[17] H. Canière, B. Bauwens, C. T'Joen, and M. De Paepe, "Mapping of Horizontal Refrigerant Two-Phase Flow Patterns Based on Clustering of Capacitive Sensor Signals," *Int. J. Heat Mass Transf.*, vol. 53, no. 23–24, pp. 5298–5307, Nov. 2010.

[18] R. Suliman, L. Liebenberg, and J. P. Meyer, "Improved Flow Pattern Map for Accurate Prediction of the Heat Transfer Coefficients During Condensation of R-134a in Smooth Horizontal Tubes and Within the Low-Mass Flux Range," *Int. J. Heat Mass Transf.*, vol. 52, no. 25–26, pp. 5701–5711, Dec. 2009.

[19] E. Van Rooyen, M. Christians, L. Liebenberg, and J. P. Meyer, "Probabilistic Flow Pattern-Based Heat Transfer Correlation for Condensing Intermittent Flow of Refrigerants in Smooth Horizontal Tubes," *Int. J. Heat Mass Transf.*, vol. 53, pp. 1446–1460, Mar. 2010.

[20] S. Lips and J. P. Meyer, "Experimental Study of Convective Condensation in an Inclined Smooth Tube. Part II: Inclination Effect on Pressure Drops and Void Fractions," *Int. J. Heat Mass Transf.*, vol. 55, no. 1–3, pp. 405–412, Jan. 2012.

[21] S. Lips and J. Meyer, "Stratified Flow Model for Convective Condensation in an Inclined Tube," *Int. J. Heat Fluid Flow*, vol. 36, pp. 83–91, 2012.

[22] R. E. Rayle, "An investigation of the influence of orifice geometry on static pressure measurements," MIT, 1959.

[23] REFPROP, *NIST Thermodynamic Properties of Refrigerants and Refrigerant Mixtures, Version 8.0, NIST Standard Reference Database 23. National Institute of Standards and Technology. Gaithersburg, MD.* Gaithersburg, MD: National Institute of Standards and Technology, 2005.

[24] K. De Kerpel, B. Ameel, S. De Schampheleire, C. T'Joen, H. Canière, and M. De Paepe, "Calibration of a capacitive void fraction sensor for small diameter tubes based on capacitive signal features," *Appl. Therm. Eng.*, vol. 63, no. 1, pp. 77–83, 2014.

[25] S. Z. Rouhani and E. Axelsson, "Calculation of Void Volume Fraction in the Subcooled and Quality Boiling Regions," *Int. J. Heat Mass Transf.*, vol. 13, pp. 383–393, 1970.

[26] E. dos Reis and L. Goldstein, "A Procedure for Correcting for the Effect of Fluid Flow Temperature Variation on the Response of Capacitive Void Fraction Meters," *Flow Meas. Instrum.*, vol. 16, pp. 267–274, 2005.

[27] E. Van Rooyen and M. Christians, "Time Fractional Analysis of Flow Patterns During Refrigerant Condensation," University of Pretoria, 2007.

[28] L. Wojtan, T. Ursenbacher, and J. R. Thome, "Investigation of Flow Boiling in Horizontal Tubes: Part I—A New Diabatic Two-Phase Flow Pattern Map," *Int. J. Heat Mass Transf.*, vol. 48, no. 14, pp. 2955–2969, Jul. 2005.

[29] N. Kattan, J. R. Thome, and D. Favrat, "Flow Boiling in Horizontal Tubes. Part 3: Development of a New Heat Transfer Model Based on Flow Patterns.," *J. Heat Transfer*, vol. 120, no. 1, pp. 156–165, 1998.

[30] P. E. L. Barbieri, J. M. S. Jabardo, and E. P. Bandarra Filho, "Flow Patterns in Convective Boiling of

Refrigerant R-134a in Smooth Tubes of Several Diameters," in *5th European Thermal-Sciences Conference*, 2008.

[31] J. R. Thome, J. El Hajal, and A. Cavallini, "Condensation in Horizontal Tubes, Part 2: New Heat Transfer Model Based on Flow Regimes," *Int. J. Heat Mass Transf.*, vol. 46, no. 18, pp. 3365–3387, Aug. 2003.

[32] M. A. Woldesemayat and A. J. Ghajar, "Comparison of Void Fraction Correlations for Different Flow Patterns in Horizontal and Upward Inclined Pipes," *Int. J. Multiph. Flow*, vol. 33, no. 4, pp. 347–370, Apr. 2007.

[33] A. Cavallini, D. Del Col, L. Doretti, M. Matkovic, L. Rossetto, C. Zilio, and G. Censi, "Condensation in Horizontal Smooth Tubes: A New Heat Transfer Model for Heat Exchanger Design," *Heat Transf. Eng.*, vol. 27, no. 8, pp. 31–38, Sep. 2006.

[34] S. P. Olivier, J. P. Meyer, M. De Paepe, and K. De Kerpel, "The influence of the inclination angle on void fraction and heat transfer during condensation inside a smooth tube," University of Pretoria, 2015.